USING SUPERDARN TO PREDICT POLAR IRREGULARITIES THAT CAUSE GPS SCINTILLATION

By

Michelle R. Simon, B.S.

A Thesis Submitted in Partial Fulfillment of the Requirements for the Degree of

Master of Science

In

Electrical Engineering

University of Alaska Fairbanks

December 2016

APPROVED:

Dr. William Bristow, Committee Chair
Dr. Joe Hawkins, Committee Member
Dr. Denise Thorsen, Committee Member
Dr. Charlie Mayer, Chair
Department of Electrical Engineering
Dr. Douglas Goering, Dean
College of Engineering and Mines
Dr. Michael Castellini, *Dean of the Graduate School*

Abstract

High levels of scintillation caused by strong magnetic storms can cause GPS devices to lose connection with the necessary satellites. Current research has shown a correlation between major magnetic storms and higher levels of the recorded Total Electron Content (TEC) seen in GPS receivers. The research presented in this thesis examines the idea that observations from the Super Dual Auroral Radar Network (SuperDARN) can be used to predict scintillation levels in GPS receivers at polar latitudes by using GPS scintillation values σ_ϕ and S_4 that were collected from January, 2013 till November, 2015. These values were gathered from Poker Flat, Alaska, and McMurdo Station, Antarctica. Using various graphical methods the GPS data was compared with the recorded velocity, power and spectral width measurements from Kodiak, Alaska, and South Pole, Antarctica, SuperDARN sites. The SuperDARN values were ignored in the comparison if they did not fall within the specified GPS field of view, they were tagged with a ground scatter flag, or the data quality flag indicating they were erroneous. These bar and scatter graphs indicate that many of the irregularities identified by SuperDARN do not cause scintillation of a GPS signal. When the GPS scintillation variables are examined as a function of the SuperDARN signal parameters (power, velocity, and spectral width) only a small dependence is shown, demonstrating little correlation between the GPS scintillation variables and SuperDARN's variables. Based on these results SuperDARN cannot be used to predict higher levels of GPS scintillation in polar latitudes.

Table of Contents

Page

List of Figures

Page

Chapter 1 Introduction

1.1 Introduction

One signal in wide use today, which can be adversely impacted by ionospheric scintillation, is that used by the Global Positioning System (GPS). Every signal sent by a GPS satellite traveling to a ground receiver can be affected by scintillation caused by ionospheric irregularities with scales between a few hundred meters to several kilometers. The accuracy of the location calculated by a GPS ground receiver depends on the quality of the signal received from the GPS satellites. This accuracy is compromised when the signal is altered by scintillation. Space physics researchers have deployed and maintain a network of receivers to determine where GPS users might be affected by scintillation. These "scintillation receivers" continuously track the level of amplitude and phase scintillation and can provide real-time space weather reports for GPS users. Space weather describes the magnetospheric disturbances from solar events that can affect the near-earth environment.

At polar latitudes, the GPS scintillation receiver network has many gaps because of the lack of population centers or simply the lack of solid ground (in the Arctic Ocean for example). These gaps mean that this network has a limited field of view. Also since polar irregularities are typically more transient than irregularities located at equatorial latitudes, frequently they can go unobserved by the network.

To understand the impact of GPS scintillation, some background information on GPS is in order. In early 1978, the first GPS satellite was launched. GPS was developed over many years by the Department of Defense (DoD), creating a satellite system that provides position and timing information for various applications. Today, the GPS satellite system is a constellation consisting of approximately 30 satellites arranged in 6 orbital planes with a minimum of 4 satellites per plane. The system operates passively, meaning there is no form of feedback from receivers to the satellites. This allows an unlimited number of users to have system access in order to calculate their position.

All GPS satellites contain an atomic clock that is precisely synchronized with that of all the other satellites in the constellation. The satellites transmit a coded signal that provides the receivers on the ground precise time and frequency information. Once three or more satellites connect to the receiver, the time stamps are used to determine the location of the receiver. If

there are less than three satellite signals connected to the receiver, triangulation is not possible. GPS has become a critical navigational system and any disruption of the signal can be detrimental.

Since GPS relies on precise timing of the signal propagation from the satellite to the ground, ionospheric scintillation, which decreases the precision with which the timing can be determined, can disrupt a GPS receiver's triangulation process. The GPS industry has defined two variables to characterize the two types of fluctuations. The first variable is the scintillation index and the second is sigma phi.

The scintillation index, or S_4, characterizes fluctuations in the signal's amplitude, which are due to diffractive scintillations. It is the normalized variance of intensity of the signal. This index is used outside of the polar regions as the primary indication of scintillation. Near the polar latitudes, ionospheric densities typically are smaller than equatorial densities and therefore tend not to produce large-amplitude diffractive scintillations.

The second variable, sigma phi index, or σ_ϕ, indicates refractive scintillation in the signal phase and is the phase deviation component of the GPS signal that is introduced during transit. Refractive scintillation can be caused by the ionospheric irregularities occurring at polar latitudes. Therefore, at polar latitudes σ_ϕ is used to measure scintillation.

A third possible cause of GPS signal disruption is temporal variations in the total electron content (TEC). TEC is the number of free electrons in a rectangular solid with a square meter cross section that extends from the receiver to the satellite. This ionospheric interference can cause the signal's travel time to be miscalculated. This miscalculated value will produce an incorrect distance between the transmitter and receiver. To correct for varying TEC levels, the GPS satellite transmits two different signals at two different frequencies simultaneously. This allows a receiver to measure the TEC and correct for its effects.

1.2 Scintillation

Scintillation is defined as fluctuations of the amplitude or phase of a signal. An example of scintillation is the "twinkle" you can see when observing stars. This is a form of atmospheric scintillation caused by the occurrence of turbulent eddies along the wave propagation path through the atmosphere. When scintillation occurs in the ionosphere, it can be highly

detrimental due to its disruptive influence upon electromagnetic waves. Electromagnetic waves are the basis of all satellite communication.

Electromagnetic waves are propagating waves carrying energy in their oscillating electric and magnetic fields. The electric field can be expressed as

$$E = E_0 \cos(\omega t - \beta z), \tag{1}$$

where E_0 is the amplitude of the electric field, ω is the frequency of the wave, z is the distance coordinate in direction of wave propagation, and β is the phase constant, which is determined by the wavelength and velocity of propagation.

The phase constant is given by

$$\beta = \omega\sqrt{\mu\epsilon}. \tag{2}$$

μ and ε are properties of the medium in which the wave propagates; μ is the magnetic permeability and ε is the electric permittivity.

In most materials μ has the same value as that of free space. However *ε* can vary significantly between common media. In the atmosphere, ε depends on environmental parameters such as temperature and electron density. In ionospheric regions where turbulence creates ionospheric irregularities, the electron density can vary significantly from place to place, resulting in irregular ε. When electromagnetic waves encounter these areas, irregular propagation paths can occur, causing scintillation.

Scintillation occurring in radio signals was first discovered during Appleton and Barnett's studies of the upper atmosphere in 1925 [1]. These early experiments proved that there is a region in the upper atmosphere where the gases are lightly ionized. This region was named the ionosphere. Appleton proceeded to develop an equation that describes the refractive index, *n*, through the ionosphere.

$$n = \sqrt{\epsilon_r \mu_r}, \tag{3}$$

where ε_r is the relative electric permittivity and μ_r is the relative magnetic permeability. For ionospheric conditions μ_r is equal to 1 simplifying the equation to $n = \sqrt{\varepsilon_r}$. The refractive index in the ionosphere shows the changes in velocity of a wave as it passes through various ionized media.

Scintillation happens on the Fresnel scale, F, which is defined as

$$F = (\lambda Z/2\pi)^{1/2}, \tag{4}$$

where λ is the wavelength and Z is the distance between the irregular medium and the receiver. By using the Fresnel scale, scintillation can be further defined into two separate types. One type is termed as diffractive scintillation which is defined as when irregularities scale size is less than or equal to F. Conversely, if the irregularity scale size is larger than F the scintillation is termed refractive. It is not uncommon for many ionospheric scintillation events to begin with diffractive scintillation, progress into refractive scintillation, and then diminish to diffractive scintillation.

Refractive scintillation occurs when the changes in the refractive index cause variations in the wave's propagation path. These variations cause the ionospheric irregularity to behave like a large lens as the GPS signals pass through it. This refractive lensing can focus or defocus the signal (see Figure 1), which alters the amplitude of the wave.

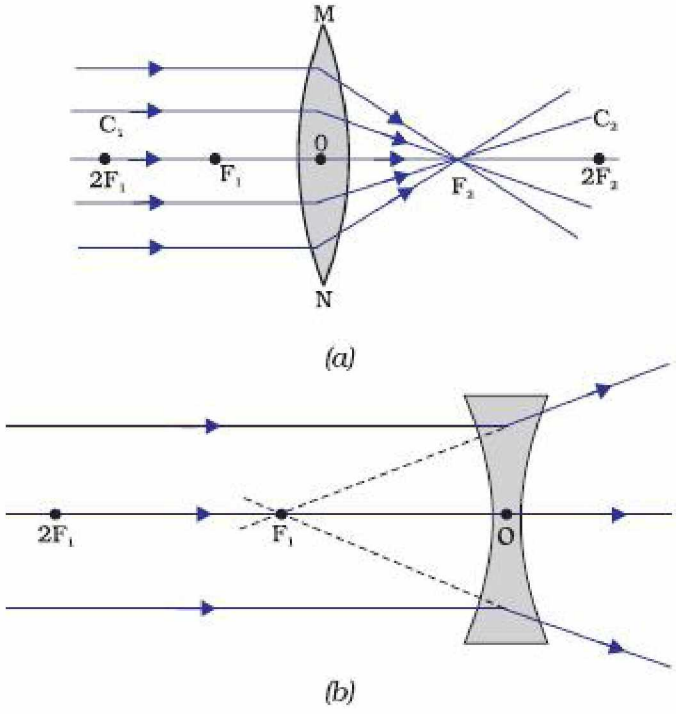

Figure 1: Focusing (a) and defocusing (b) of a wave through a lens [2]

Diffractive scintillation occurs when a wave evolves as it travels through irregularities, with scales comparable to F, causing small changes of phase along the wavefront. As the wave propagates beyond the irregularities, constructive and destructive interference from

superposition of different portions of the wavefront causes amplitude scintillation. The amount that the wave's phase, ϕ, shifts is based on the electron content, I, within the area it passed through. This can be described as

$$\phi = (8.45 * 10^{-7})I/f, \tag{5}$$

where f is the frequency of the wave (Hz).

The electron content is the density of electrons, N, in a column of unit cross-section along the propagation path, dl, or

$$I = \int N\, dl. \tag{6}$$

1.3 Overview

The second chapter of this thesis will expand in further detail on several points. The first is the ionosphere's composition and movement. Next, the chapter will examine the equation for the refractive index within an ionized medium. Third, the types of ionospheric irregularities that occur in the polar latitudes will be discussed. Then fourth, SuperDARN's setup and why it is believed it can be used to identify the irregularities that affect GPS signals will be examined. Finally, a literature review will be included to document the previous research.

The third chapter will discuss the GPS and SuperDARN sites from which data were collected, how the GPS and SuperDARN instruments are configured at each site, what type of data were accessed, where they were stored, and an analysis of results of this investigation.

The concluding chapter will give a general overview.

Chapter 2 Background Research

2.1 Ionosphere

The development of communication systems led to the discovery of the ionosphere. Although, the ionosphere was previously theorized to exist, the first real indication was in 1901, during Marconi's trans-Atlantic communication experiment between Cornwall and Newfoundland [1]. At the time it was hypothesized that due to the curvature of the earth, the wave could not reach Newfoundland unless it was reflected off atmospheric charged particles. The upper atmospheric region in which these charged particles are concentrated became known as the ionosphere. Through further studies, it was later discovered that the ionosphere is made of free electrons and positive ions that are typically in equal numbers, making the medium electrically neutral. Although there are fewer charged particles than neutral particles, there are enough of them to refract high frequency electromagnetic waves transmitted from the ground back toward earth and enable long-distance over the horizon communication.

The ionosphere is created by ionization of the neutral atmosphere, primarily through the absorption of photons from the Sun's extreme ultraviolet (EUV) and X-ray radiation. The highest concentration of ions happens during the day around noon at or near the equator. This occurs because, at the equator, the angle at which rays from the sun are incident on the atmosphere is nearly 90° and photons travel the shortest possible distance through the atmosphere to reach a certain altitude. Conversely, near the poles where the incidence angles are oblique, the distance traveled through the atmosphere to reach an altitude is longer than at the equator and less photons are available to produce ionization. At high latitudes energetic particles precipitating from the magnetosphere impact the neutral gas creating the aurora and provide another ionization source. Once an ion is created, multiple chemical processes act upon it and either remove it or convert it to another species. For example, ionization of atomic oxygen produces oxygen ions, which can react with nitrogen molecules to create nitrogen-oxide ions and atomic nitrogen. This continual process of ionization and chemical reaction creates the ionospheric layers.

The ionosphere can consist of four layers. They are the D layer (60 - 90 km), the E layer (90 - 160 km), the F1 layer (160 - 180 km), and the F2 layer which has a maximum height of

around 300 km. The maximum value of the electron density in these layers increases with height, typically starting at about 10^9 m^{-3} in the D layer and reaching a maximum of as much as several times 10^{12} m^{-3} in the F2 layer (see Figure 2). The D, E and F2 layers tend to exist during the day while the F1 layer's existence is sporadic. During the night, due to the lack of direct solar extreme ultraviolet radiation, the D and the F1 layers disappear. During this same time the E layer loses most or all of its density. The F2 layer is the longest lasting, slowly losing density through the night.

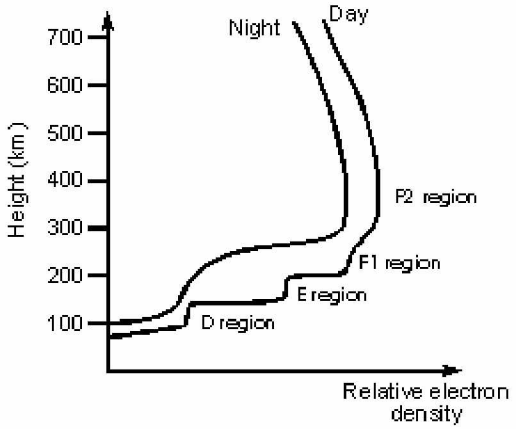

Figure 2: Ionospheric layers [3]

The ion-electron gas of the ionosphere constitutes a plasma, which is a gas of electrically charged particles that exhibits collective properties and is affected by electric and magnetic fields. In the upper E layer and in the F layer, the motion of the plasma is largely controlled by the Earth's magnetic field, while at lower altitudes collisions between the plasma constituents and the neutral atmosphere determine the motion. Electric fields imposed on the ionosphere from the magnetosphere drive motion of the plasma perpendicular to the magnetic field. The electric field is created at polar latitudes through the interaction between the Earth's magnetic field, the solar wind, and the Interplanetary Magnetic Field (IMF). Changes in the electric field can cause plasma instabilities that lead to the irregular structure of the ionospheric plasma.

The solar wind is a plasma that originates in the Sun's upper atmosphere. It streams away from the sun, moving radially outward into interplanetary space. The solar wind's kinetic energy density is significantly greater than the Sun's magnetic field energy density, hence solar magnetic field lines, the IMF, are dragged along with the plasma. As the solar wind propagates outward it encounters the Earth's magnetic field and interacts with it. If an IMF line is directed

southward when it reaches the Earth's magnetic field lines, which are directed northward, the two fields can merge (see (a) on Figure 3). This process causes Earth's outer field lines to disconnect on Earth's dayside and be drawn along with the solar wind across the pole to the nightside where they reconnect (see 1-5 on Figure 3). In this reconnection, solar wind plasma becomes attached to the Earth's magnetic field lines (see 6 on Figure 3). This attached plasma can precipitate into the atmosphere, colliding with neutral particles, and thus creating ionospheric plasma at polar latitudes. These lines, once reconnected, push back towards the Earth, creating a circulation of magnetic flux within the magnetosphere referred to as magnetospheric convection. The field lines flow back to Earth's dayside (see 7-9 on Figure 3) where they can again merge with the IMF. This circulation pattern maps along field lines into the upper atmosphere at high latitudes and drives ionospheric plasma motion of several hundred meters per second or more (see (b) on Figure 3).

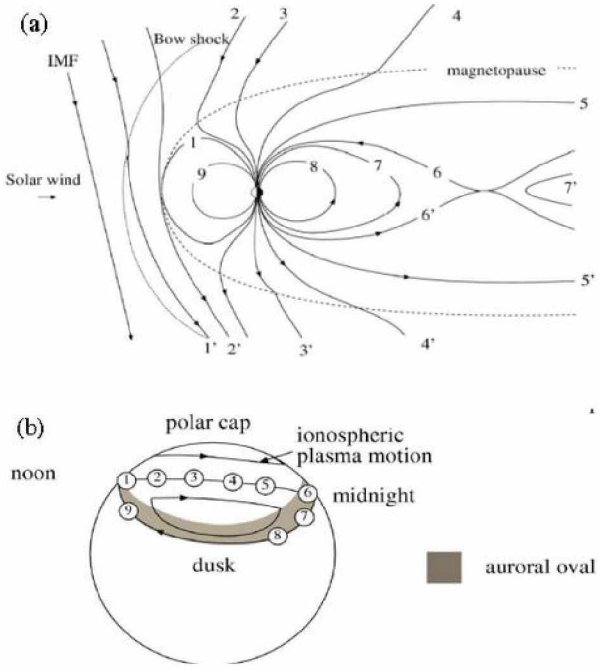

Figure 3: Reconnection process [4]

2.2 Index of Refraction

As previously mentioned, Appleton created an equation that solves for the index of refraction, n, of an electromagnetic wave in an ionized medium. This equation describes a complex refractive index, where both the amplitude and phase of the electromagnetic wave can be affected by the changes in the characteristic frequency within the ionosphere. The

equation is expressed in terms of three dimensionless quantities: X, Y, and Z (see Equations 9 - 11). There are three main characteristic frequencies within the ionosphere: the plasma frequency (ω_n), the gyrofreqeuncy (ω_B), and the electron collision frequency (v). The quantities X, Y, and Z are ratios between the electromagnetic wave frequency, ω, and one of the characteristic frequencies of the ionosphere.

The plasma frequency, ω_N, is the natural frequency of oscillation for the electrostatic perturbations within the plasma, described as

$$\omega_N = \sqrt{\frac{Nq^2}{\epsilon_o m_e}}. \tag{7}$$

The gyrofrequency, ω_B, is the frequency of the gyration of an electron traveling in a magnetic flux density, B. The frequency of gyration is described by the equation

$$\omega_B = \frac{Bq}{m_e}. \tag{8}$$

In Equation 7, N represents the electron density (m^{-3}). In both Equation 7 and 8, q is the charge of the electron (C) and is taken to be positive, m_e is the mass of the electron (kg), ε_o is the permittivity of free space (F/m) and B is the magnetic flux density of the medium (Wb/m).

The collision frequency, v, is the rate of collision between a given electron and other particles. There is not a simple analytic expression for v. Rather, it is described by complex expressions given by the kinetic theory of gasses.

Together, these three characteristic frequencies divided by the electromagnetic wave frequency define the dimensionless quantities

$$X = \frac{\omega_N^2}{\omega^2}, \tag{9}$$

$$Y = \frac{\omega_B}{\omega}, \tag{10}$$

and

$$Z = \frac{v}{\omega}. \tag{11}$$

With these definitions, the Appleton equation is:

$$n^2 = 1 - \frac{X}{1 - jZ - \frac{Y_T^2}{2(1-X-jZ)} \pm (\frac{Y_T^4}{4(1-X-jZ)^2} + Y_L^2)^{1/2}}. \quad (12)$$

In this equation, Y is divided into longitudinal and transverse components defined as

$$Y_L = Y \cos\theta, \quad (13)$$

and

$$Y_T = Y \sin\theta. \quad (14)$$

For this, θ is the angle between the direction of propagation and the magnetic field. The refractive index is used to predict electromagnetic wave interactions with areas of differing ionospheric frequency influences.

2.3 Types of Irregularities

The polar latitude ionosphere is highly dynamic. It contains areas with sharp transitions between sections of irregularities created by energetic particle precipitation and by plasma instabilities caused by the electric field imposed by the magnetosphere. At these latitudes there are two main types of large-scale irregularities.

The largest scale irregularities within the polar latitudes are called patches [5]. Patches in the horizontal direction (parallel to the Earth's surface) range from a few 100 km to 1000 km. They are located mainly in the F layer of the ionosphere during the winter. This plasma detaches from the dayside subauroral ionosphere (see Figure 4). It is then transported from lower latitudes of the dayside ionosphere through the polar cap into the nightside of the auroral region. Magnetosphere interactions with the changing IMF causes the plasma flow's velocity to vary wildly, creating irregularities.

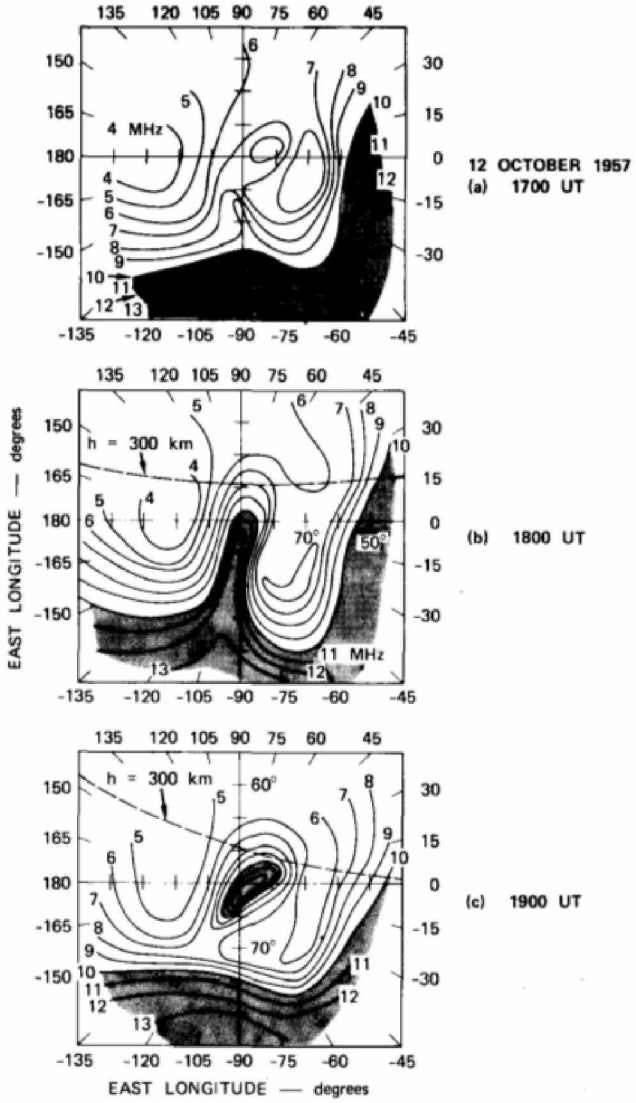

Figure 4: The development of a patch when the irregularity from the dayside subauroral ionosphere (isolated black region in Figure 3a) becomes detached and starts to move through the polar cap [5]

The second type of large-scale irregularities are called blobs [5]. They are approximately 100 km or less in the horizontal dimension. These blobs also occur in the F layer. They are created by the breakup of patches when they enter the dayside convective flow. Their main characterizations are steep density gradients transverse to the geomagnetic field. During years of high solar activity blobs tend to dominate the structural properties of the polar F layer. Both patches and blobs can be created and/or affected by instabilities.

The main instability acting at polar latitudes is the $\vec{E}$ x $\vec{B}$ instability [5]. This instability starts when there is an electric field perpendicular to a plasma density gradient (see Figure 5).

This configuration creates an unstable geometry with secondary polarizing electric fields that reinforces the growth of irregularities. $\vec{E}$ x $\vec{B}$ instabilities exist throughout the ionosphere.

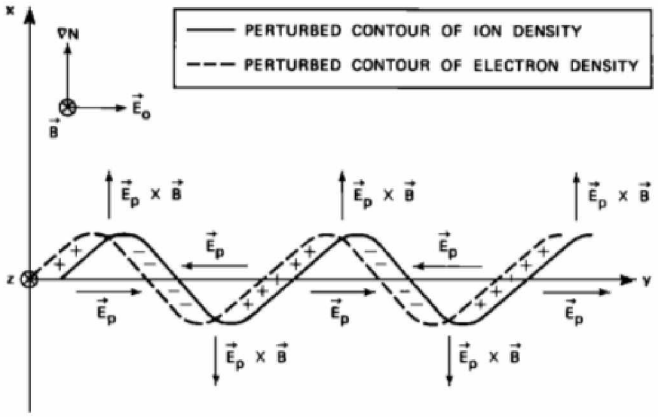

Figure 5: Simplified schematic diagram showing the basic mechanics of the $\vec{E}$ x $\vec{B}$ instability [5]

$\vec{E}$ x $\vec{B}$ instabilities start when ions begin to slightly drift (Figure 5 represented by the solid curve) across plasma density contours, leaving the electrons strongly attached to the magnetic field line (Figure 5 dashed curve), causing a charge separation, and thus creating a positive feedback loop. The charge separation creates the polarization electric field, E_p, which reinforces the initial perturbation causing the irregularity to grow along the existing gradient. The $\overrightarrow{E_p}$ x $\vec{B}$ motion causes regions with less dense plasma to move into areas of denser plasma and vice versa. This movement can change the electron density in irregularities, creating even smaller pockets of differential electron density within the larger irregularity.

2.4 SuperDARN

The Super Dual Auroral Radar Network (SuperDARN) observes signals scattered from ionospheric irregularities that are related to the irregularities that adversely impact GPS signals. SuperDARN is a network of High Frequency (HF) radars that observe the mid and high-latitude regions of both the northern and southern hemispheres. The radar's field of view covers many of the regions where there are gaps in the current GPS network. This could potentially allow for the use of SuperDARN to identify regions where GPS receivers could experience scintillation.

SuperDARN is a network of coherent scatter radars that started operating during the 1990's. Originally conceived in the early 1980's at the Johns Hopkins University Applied Physics Laboratory, today the network consists of over 30 low-power high-frequency radars. The

primary targets of SuperDARN are magnetic field-aligned plasma density irregularities in the ionosphere's E and F layers. The radars operate continuously in order to observe plasma motion in the ionosphere. SuperDARN is proving successful for studying dynamic processes in the Earth's magnetosphere, ionosphere, and neutral atmosphere.

This paper's main interest is comparing SuperDARN observations of signals scattered from ionospheric irregularities with the scintillation of GPS signals caused by irregularities. SuperDARN scattering can be understood in terms of the reflection coefficient, Γ, that occurs between regions of differing plasma density. The reflection coefficient shows the percent of the wave that is reflected by the successive ionospheric irregularities:

$$\Gamma = \frac{n_1 - n_2}{n_1 + n_2}. \tag{15}$$

The refractive indices of the irregularities are described as n_1 and n_2. The parameters of the returned signals from these multiple reflections are used to calculate power, drift velocity, and spectral width.

The signal power is simply the sum of the squares of the in-phase and quadrature components of the received signals. To compensate for variations in the propagation conditions, SuperDARN reports power as dB above the received noise level.

Drift velocity is determined from the Doppler shifts of the returned signals. Doppler shifts are the difference between the transmitted frequencies and the received frequencies. The drift velocity calculations identify the bulk movement of ionospheric plasma.

Spectral width measures the decay of the real and imaginary parts of the autocorrelation of the returned signal. It is a measure of the time over which the signals remain correlated.

If the returned wave has a low velocity and a narrow spectral width, it is flagged as ground scatter. Ground scatter is a propagation mode in which the signals propagate out from the radar, reflect obliquely from the ionosphere down to the ground where they scatter and return to the radar along the same path. From a personal communication with W.A. Bristow it was mentioned that research comparing a large database of ionospheric-scatter signals with ground-scatter signal have demonstrated that ionospheric-scattered signals generally decorrelate more rapidly than ground-scattered signals and hence have broader spectra. In

addition, the ionosphere is typically in motion while the ground is not, so ground-scatter signals have low Doppler velocities. It is important to differentiate between the two signals because the ionospheric-scatter signals indicate the presence of ionospheric irregularities, while ground-scatter signals do not.

2.5 The Effect of Irregularities on SuperDARN and GPS Signals

All SuperDARN sites are designed to operate within the High Frequency band, which is the range of frequencies between 3-30 MHz. SuperDARN operates between 8-20 MHz, with the Kodiak site often operating around 10 MHz and the South Pole site around 12 MHz. SuperDARN radars receive coherent-backscatter, which is due to Bragg scattering from irregularities of a distinct size, d

$$d = \frac{\lambda}{2\sin\theta}. \tag{16}$$

For SuperDARN, the angle of incidence, θ, is 90 degrees, simplifying Equation 16 to $d = \frac{\lambda}{2}$. λ is the signal's wavelength given by

$$\lambda = \frac{c}{f}, \tag{17}$$

with c being the speed of light (m/s), and f the frequency of the signal (Hz). Bragg scattering is where the returned wave is composed of the partial reflections of the original signal from multiple scattering centers, with constructive interference occurring when the distance between each scattering center is half of the radar's transmitting wavelength. Therefore, the size of irregularities measured by SuperDARN for both Kodiak and South Pole are between 12 to 15 meters.

GPS satellites operate within the Ultra High Frequency band between 300-3000 MHz. While signals in this band are less susceptible to scintillation than lower frequency signals would be, they still can be affected. To help offset the impact of scintillation, GPS utilizes two different frequencies within the Ultra High Frequency band to allow for some correction of the possible interference. L_1 is defined as 1575.4 MHz and L_2 defined as is 1227.6 MHz.

As discussed in Section 1.2, irregularities in the ionosphere cause changes of phase along the wavefront of GPS signals. The greatest possibility of a GPS signal degradation occurs when the signal travels through an irregularity whose size range is comparable to the size of the

Fresnel zones of the propagation path between the receiver and the satellites. Fresnel zones are oval regions determined by comparing the distance along chords of the oval to the distance on the straight line connecting the transmitter and receiver (see Figure 6). The length of the path along the chords defining the first Fresnel zone is one half wavelength longer than the direct path.

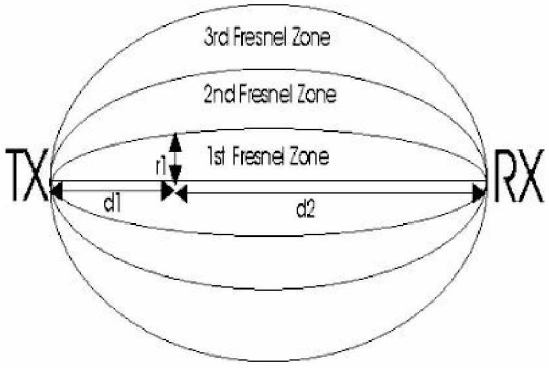

Figure 6: Fresnel zones where r1 is equal to r_F [6]

Any part of the signal that arrived at the receiver along the chords of the first Fresnel zone, would be 180° out of phase with the signal that arrived along the direct line of sight path. The two components of the signal would destructively interfere, reducing the signal amplitude. Any part of the signal that arrived along chords of the second zone would lead to constructive interference and increase the signal amplitude. Hence, the amplitude of any signal passing through a region of irregularities with sizes comparable to the Fresnel zone radii at ionospheric altitudes would fluctuate depending on which paths dominate at any given time. The signal's phase would fluctuate as well since it is determined by the summation of the phases of the signal components arriving along the various paths.

The first Fresnel zone's radius is defined as

$$r_F = \sqrt{2\lambda r}. \tag{18}$$

For this equation λ is the wavelength (m) and r is the distance from the irregularity to the receiver (m).

By using the Fresnel radius, a spectrum of the amplitude deviation or the Fourier transform of the intensity auto correction function, ϕ_I, of a GPS signal can be described as

$$\phi_I(k_x) = \phi_\phi(k_x)\sin^2\left(\frac{k_x^2 r_F^2}{8\pi}\right). \tag{19}$$

The spectrum of the phase deviation, ϕ_P is

$$\phi_P(k_x) = \phi_\phi(k_x)\cos^2(\frac{k_x^2 r_F^2}{8\pi}). \quad (20)$$

In these equations, k_x is the horizontal wave number of the phase fluctuations and ϕ_ϕ is the power spectrum of the wave phase exciting the screen. The wave number, k, which is

$$k = \frac{2\pi}{\lambda}. \quad (21)$$

The wave number is often written as a vector indicating the propagation direction.

From these equations Fresnel filtering zones are derived. They indicate the upper limits on the size of the irregularities that affect the GPS signal, namely $\sin^2(\frac{k_x^2 r_F^2}{8\pi})$ and $\cos^2(\frac{k_x^2 r_F^2}{8\pi})$. These upper limits are found when the $\sin^2$ term goes to 1, occurring when the angle is equal to $(2n-1)\pi/2$ radians, or when $\cos^2$ goes to 0, which occurs when the angle is equal to πn radians. Based on these equations it was determined that the size of irregularities that will cause scintillation for GPS signals are on the scale of decameters to kilometers, which correspond to the plasma blobs and patches discussed in Section 2.3 [7].

The plasma instabilities described in Section 2.3 create turbulent cascades within large irregularities resulting in a spectrum of smaller irregularities. In a power spectrum plot such as that shown in Figure 7, the range of irregularities that make up the larger irregularity can be identified [8]. The spectra show a power-law distribution, k^{-p}, where k is the wave number.

For these plots the vertical axis is the log of the change of the refractive index. The horizontal axis is either the frequency or the wave number of the system. Figure 7 shows an example spectrum, and indicates the range of ionospheric irregularities that can affect various frequencies. As mentioned earlier, SuperDARN scatters off of irregularities that are between 10 to 15 meters in scale, making the wave number around 10^{-1} m^{-1}. As the figure demonstrates, irregularities of this scale can be embedded within the irregularities that cause the GPS scintillations that have wave numbers between 10^{-1} through 10^{-4} m^{-1}.

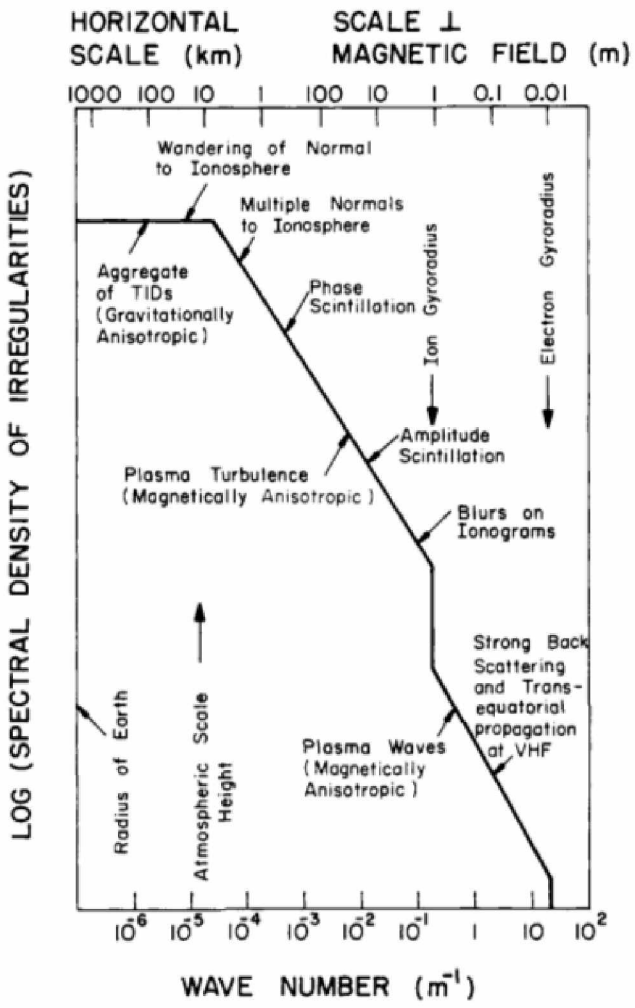

Figure 7: A composite spectrum summarizing the intensity of ionospheric irregularities as a function of wave number over a spatial scale from the electron gyro-radius to the radius of the Earth [8].

2.6 Literature Review

There is a large body of research characterizing ionospheric irregularities and their impacts on GPS and other satellite systems. In this section, some of the relevant publications are reviewed. As is true with most ionospheric research, the publications and the description here are divided into geophysical regions based upon latitude. The reason for this is that the processes driving the creation of scintillation causing irregularities and the characteristics of the irregularities are both strongly latitude dependent.

Low latitudes are defined as between the magnetic equator and about ±15° [9]. GPS scintillations in this region are typically associated within the equatorial F-region ionosphere. Early observations of the equatorial ionosphere using an instrument known as an ionosonde

exhibited a “spread” in range or frequency [9]. This ionosonde signature became known as Equatorial Spread F (ESF) and it is associated with irregularities that cause the majority of the GPS scintillations. ESF typically develops after sunset and propagates both upwards and to off-equatorial latitudes. Another cause of scintillation is the density gradients within “plumes” that are formed in this region by convective instabilities driven by gravitational forces [9].

Midlatitude regions are between ±15° latitude to ±60° latitude. In this region GPS scintillations occur infrequently and are typically associated with magnetic storms that occur during solar maxima [7].

Intense diffractive scintillations are often observed at high latitudes in the Very High Frequency (VHF) and Ultra High Frequency (UHF) bands [10]. These scintillations are produced by ionospheric irregularities created in the F region by density gradients that are associated with polar cap patches. These irregularities are typically observed in the polar cap poleward of the auroral zone.

Phase fluctuations are a form of refractive scintillation and are observed to be the largest in the auroral oval near the magnetic midnight. At polar cap latitudes phase fluctuations are less intense. The fluctuations increase in intensity during periods of magnetic activity, moving equatorward along with the auroral oval [7].

During moderate geomagnetic storms, increases in scintillation are observed throughout the world. At polar latitudes the most intense scintillation are located at the polar cap and cusp. In a study by Prikryl et al. published in 2013 [11] the ionospheric backscatter, observed by PolarDARN radars (SuperDARN radars located at polar latitudes owned by Canada) and CADI ionosondes, was associated with areas of decameter F-region irregularities while scintillation was observed on GPS receivers. The irregularities were located within a dense tongue of ionization and polar cap patches. This tongue is drawn across the polar cap by ionospheric convection with possible speeds exceeding 1500 m/s [11].

Research by Kinrade et al. published in 2013 [12] found correlation between GPS signal fluctuations and auroral emissions and possible ionospheric irregularities. It is known that the 630.0 nm auroral emissions are associated with polar cap patch irregularities. It was proven that observed scintillation depended on the auroral intensity and the irregularities’ structure.

Also the spatial and temporal correlation with σ_ϕ was best during intense and persistent auroral activity. It was observed that there is a 63% correlation between the 630.0 nm auroral emissions and GPS phase scintillation, σ_ϕ.

As previously mentioned, HF radars are sensitive to decameter-scale irregularities. These small-scale irregularities are produced over large areas, often extending for hundreds of kilometers [13]. These irregularities are often found within patches and blobs due to the electron density gradients and the electric fields within the larger irregularity [5]. However, since small-scale irregularities exist outside of patches and blobs, other ionospheric instruments are often needed to confirm the readings are part of or within the larger irregularity. A study about tracking patches using HF radars in the South Pole was published by Roger et al. in 1999 [14]. Roger et al. [14] used a broad-beam riometer deployed at the South Pole Station along with the Halley Polar Anglo-American Conjugate Experiment (PACE) HF radar to examine the polar latitudes' ionosphere. Riometers are instruments used to determine ionospheric absorption and provide an indication of the amount of ionization in the lower layers (D&E) of the ionosphere. The riometer was able to confirm that polar patches observed by the Halley HF radar preceded the riometer polar patch signature. This paper helped to demonstrate that HF radars can detect the large-scale irregularities that can cause scintillation within a GPS signal at polar latitudes.

Chapter 3 Overview and Comparison of the Data

3.1 Introduction

The purpose of this thesis is to determine if SuperDARN data is useful for detecting the irregularities that cause GPS scintillation. By using various displays of the data, potential patterns may emerge. The graphs chosen to represent the data are varied and consist of different methods of comparing SuperDARN's velocity, power, and spectral width measurements to GPS's S_4 and σ_ϕ.

3.2 GPS Sites

In the beginning of this research the locations of each GPS and SuperDARN site needed to be examined to determine which sites could be used for the intended purpose. The first requirement was to identify each of the GPS sites where the receiver recorded scintillation data. Secondly, the GPS site also had to be within the field of view (FOV) of a SuperDARN radar. The third requirement was that the GPS site was operating during the same time period as the corresponding SuperDARN site. One specific type of GPS scintillation receiver was identifier was identified as fitting all of these requirements for each of the chosen GPS locations.

This type of GPS receiver is called a Connected Autonomous Space Environment Sensors (CASES) receivers and it has been installed at both polar latitudes within the FOV of UAF SuperDARN radars. These CASES receivers are scientific grade, low cost, dual-frequency GPS receiver developed by Cornell, the University of Texas in Austin, and Atmospheric and Space Technology Research Associates. These receivers handle data acquisition and tracking operations along with science and navigation relations, such as TEC computations and scintillation monitoring. The raw signal amplitude and phase data are output at a cadence between 10 - 100 Hz. They use a triggering strategy that ensures triggering sensitivity to both phase and amplitude scintillation. This strategy was first described by O'Hanlon et al. 2011 [15] and has shown to reliably indicate scintillation on historical data at high and low latitude regions [16]. The two GPS sites chosen for this project were located at Poker Flat, Alaska and McMurdo, Antarctica.

The GPS receivers at Poker Flat are operated by the Illinois Institute of Technology. Their system is made up of six CASES receivers with each receiver connected to its own external

antenna, reporting the scintillation indices for either frequency calculated every 100 seconds. The elevation and azimuth angles are recorded at a rate of every 1 second [17].

The system at McMurdo is maintained by the University of Bath, UK, and the British Antarctic Survey (BAS). It is a single receiver with seven other similar receivers located at other locations around Antarctica. It compares the differences between other nearby GPS scintillation receivers' measurements to detect and accurately quantify scintillation in the area. This GPS receiver makes 27 scintillation measurements per minute from 9 different satellite transmissions with each satellite's scintillation recorded for 3 different altitudes.

3.3 SuperDARN Locations

Two SuperDARN sites correspond with the aforementioned GPS sites. In the northern polar latitude the SuperDARN site at Kodiak, Alaska, intercepts the Poker Flat's GPS field of view directly (see Figure 8). At southern latitudes the South Pole SuperDARN was chosen since its beam's range goes directly over McMurdo Station, Antarctica (see Figure 9).

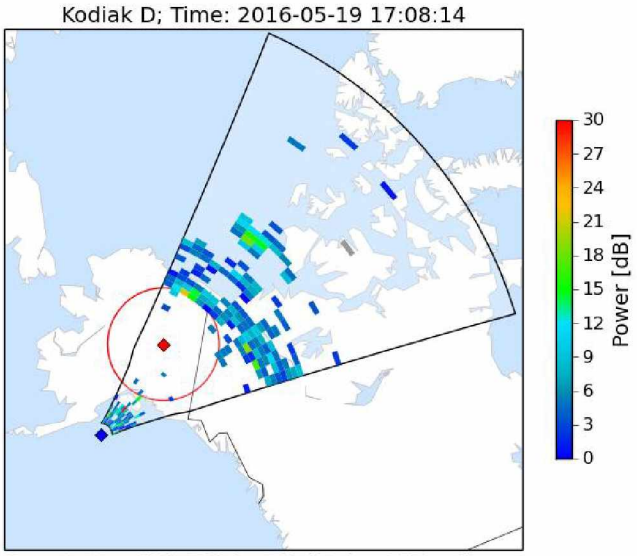

Figure 8: Poker Flat's GPS location (red diamond) and field of view (red circle) are within Kodiak SuperDARN's range

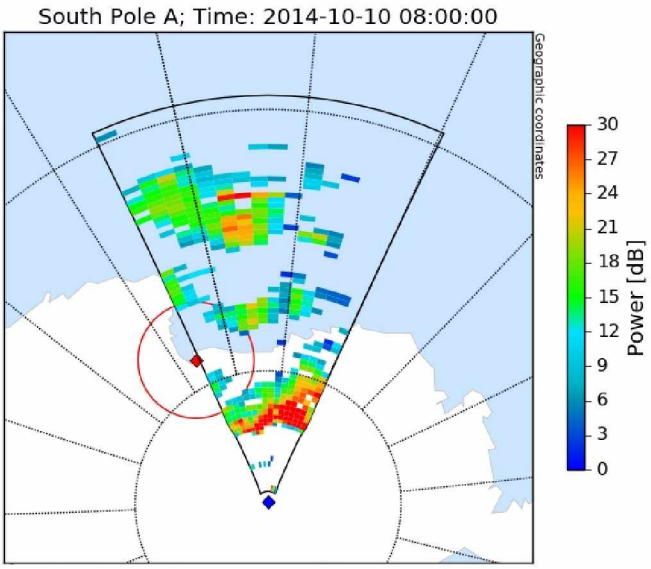

Figure 9: McMurdo Station's GPS location (red diamond) and field of view (red circle) are within South Pole SuperDARN's range

These two SuperDARN sites have similar antenna setups, using 20 log-periodic antennas that are arranged in two rows. The first row consists of 16 antennas and is the main array that transmits and receives the radar's signals. These antennas work as a phased array system and employ true-time-delay beam steering. The second row is composed of the 4 remaining antennas, also operating as a phased array but receive only. The signals from the two arrays are cross-correlated, creating an interferometer to give vertical angle of arrival information.

3.4 Data Recorded

The data was located on different servers and was processed from each of the locations in Alaska and Antarctica. Each location required a different script set up to ease the data download to our local computer.

Poker Flat's GPS data was downloaded using a UNIX script from a shared server owned by Illinois Institute of Technology. This script loaded each day's worth of data. There were two separate types of data files used. The first type of files was *scintdef.txt*. These files contained time-stamped scintillation measurements, S_4 and σ_ϕ. The second type of file was a *tx.txt* file, which contained the elevation and azimuth of each GPS value. This section of the data was limited by the large gaps in data seen on the shared server during 2013. The data sample ended when the graphing scripts were finalized late in 2015. These parameters created a date range of December 2013 through November 2015. But, due to the lack of GPS data stored within the

server, there is a data gap in July 2014 and December 2014.

McMurdo's GPS data was taken from the Madrigal MIT database, which is a National Science Foundation sponsored system that provides a broad range of observations of the space environment. This system allows for various GPS site queries. The query used for this project was one file per year that included the date, latitude, longitude, K_p, F10.7, $S_{4,}$ and σ_ϕ for each measurement. K_p and F10.7 are two separate indicators of solar weather to be used if solar weather information was needed. The date range for this site was limited by the installation and implementation of the South Pole SuperDARN and ended when the McMurdo's GPS site ceased operation. The files have date range from January 2013 till November 2014.

SuperDARN's data is located on a server owned by University of Alaska, Fairbanks. They are fit data files that are known as *fitacf*. This server allows a modified script, originally created from Virginia Tech, to access these data files and process them into a single variable containing a single beam's worth of data. This variable is then compared to the downloaded GPS data in each of the graphing functions.

3.5 Data Formats

This project utilized three different plot formats. For all plots the data was matched by timestamp to the closest minute. The Alaskan GPS data can have up to six scintillation values for each timestamp due to the six separate receivers. Each of these values is matched with the transmitter identification number so that the latitude and longitude of the ionospheric pierce point can be calculated. The ionospheric pierce point is the latitude, φ_I, and longitude, λ_I, where the line of sight from the receiver to the GPS satellite passes through the ionosphere (see Figure 10). The McMurdo GPS site gave the ionospheric pierce point as part of the Madrigal database data. For Poker Flat, Alaska, the ionospheric pierce point was calculated from the elevation angle, E, and azimuth angle, A, using the procedure created by John A. Klobuchar, a senior member of the IEEE Air Force Geophysics Laboratory [18]. These equations use the GPS receiver's latitude, φ_u, and longitude, λ_u.

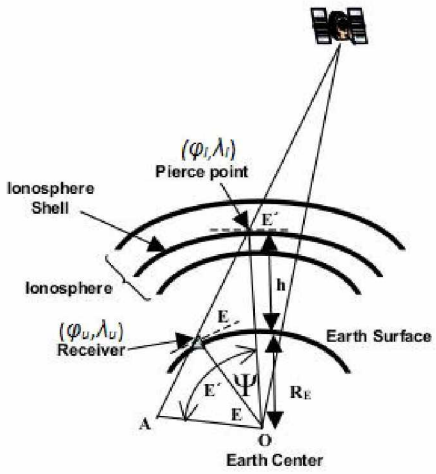

Figure 10: A diagram showing the calculation of the ionospheric pierce point *[19]*

Figure 10 illustrates the various angles used in the equation for calculating the ionospheric pierce point. The earth-centered angle, ψ, defined from the center of a spherical Earth to the receiver, is the offset between the ionospheric pierce point and the user's receiver angle and is found by

$$\psi = E' - E, \tag{22}$$

where E is the elevation angle defined at the receiver that is given by each Poker Flat's GPS timestamp. Then the elevation angle at the pierce point, E' is

$$E' = \arccos((\frac{R_E}{R_E + h}) \cos E), \tag{23}$$

where R_E is the spherical Earth's radius which has a given accepted value of 6371 km and the ionospheric height, h, which was assumed to be 350 km, a value that has been used by other researchers [19]. These equations can then be simplified to calculate ψ

$$\psi = \frac{0.0137}{E + 0.11} - 0.22. \tag{24}$$

The latitude of the ionospheric pierce point can be calculated using the previously calculated ψ, latitude of the receiver, φ_u, and the azimuth angle, A, given with each Poker Flat's GPS timestamp

$$\phi_I = \phi_u + \psi \cos A. \tag{25}$$

This set of equations was derived using a "flat-Earth" approximation, which can introduce large errors at polar latitudes when calculating the latitude and longitude of the pierce point. To compensate for the introduced error the latitudes are limited to any latitudes between ±75°. This limitation is done by controlling ϕ_I, namely by setting ϕ_I to 0.416 if $\phi_I > 0.416$ and setting ϕ_I to -0.416 if $\phi_I < -0.416$. This limits the pierce point latitude to be between ±75°. The longitude of the ionospheric pierce point can then be calculated

$$\lambda_I = \lambda_u + \frac{\psi \sin A}{\cos \phi_I}. \tag{26}$$

Once the ionospheric pierce point is calculated, the GPS data can be matched to the SuperDARN data by timestamp and the location of the point.

SuperDARN data are recorded in range gates along a beam direction, with a time stamp for each beam. Data from each range gate has a quality flag, (In a private communication with W. A. Bristow it was stated that the quality flag when set to one indicating that the fit to the raw data met a variety of criteria for quality of fit), and a ground scatter flag. These flags were used to determine if a record should be included in the analysis. Specifically, if the ground scatter flag is set or the quality data flag is unset, the value from the range gate was disregarded. All valid data points falling within a 5-range gate by 5-beam neighborhood of a GPS ionospheric pierce point at a given time were averaged to produce a single SuperDARN parameter value.

Various graphical methods were used to analyze this data. It is to be noted that at each of these sites the projection of the velocity on the radar beam directions was used and not the full velocity vector. When examining these results the data was separated out according to polar location. Data from the Northern latitudes originated from two locations found in the state of Alaska. This will be referred to as the Alaskan data. The Southern latitudes data originated from two locations in Antarctica. This will be referred to as the Antarctica data. Each plot was generated separately for both GPS scintillation values S_4 and σ_ϕ.

3.6 GPS Scintillation Occurrences vs SuperDARN Occurrences as a Function of Time

The first basic analysis used GPS scintillation data collected from a single moderate solar weather day, on which the planetary index K_p had the value 4. The analysis was completed for

both the Alaskan and the Antarctic locations to see what the typical GPS scintillation levels were (see Figure 11 and Figure 12). These figures demonstrated that even on moderate days there were changes in both S_4 and σ_ϕ that occurred at approximately the same time period in both datasets, indicating that during those time periods both GPS scintillation receiver sites registered scintillation. The most obvious change is an increase in the GPS σ_ϕ recorded in the Alaska receivers just prior to 21:00 UT. Examination of the McMurdo observations shows a similar but smaller spike in the same time frame, possibly showing similar magnetic activity causing irregularities at both poles. The data collected for Alaska's σ_ϕ appeared to have greater variation than any of the other GPS scintillation values in either location. When comparing the same day data of the GPS scatter plots and the SuperDARN range-time plots of a single radar beam, time periods showing similar increases in irregularity identification can be identified by areas of higher power and velocity values existing during periods of higher observed GPS σ_ϕ values. For Alaska the time frame between 10:00-12:00 UT and approximately 21:00 UT show increases in observed scatter. For Antarctica there is only one time period that can be seen, the period just prior to 21:00 UT, which shows simultaneous increases in SuperDARN's power and/or velocity values and GPS's scintillation values (see Figure 13 and Figure 14).

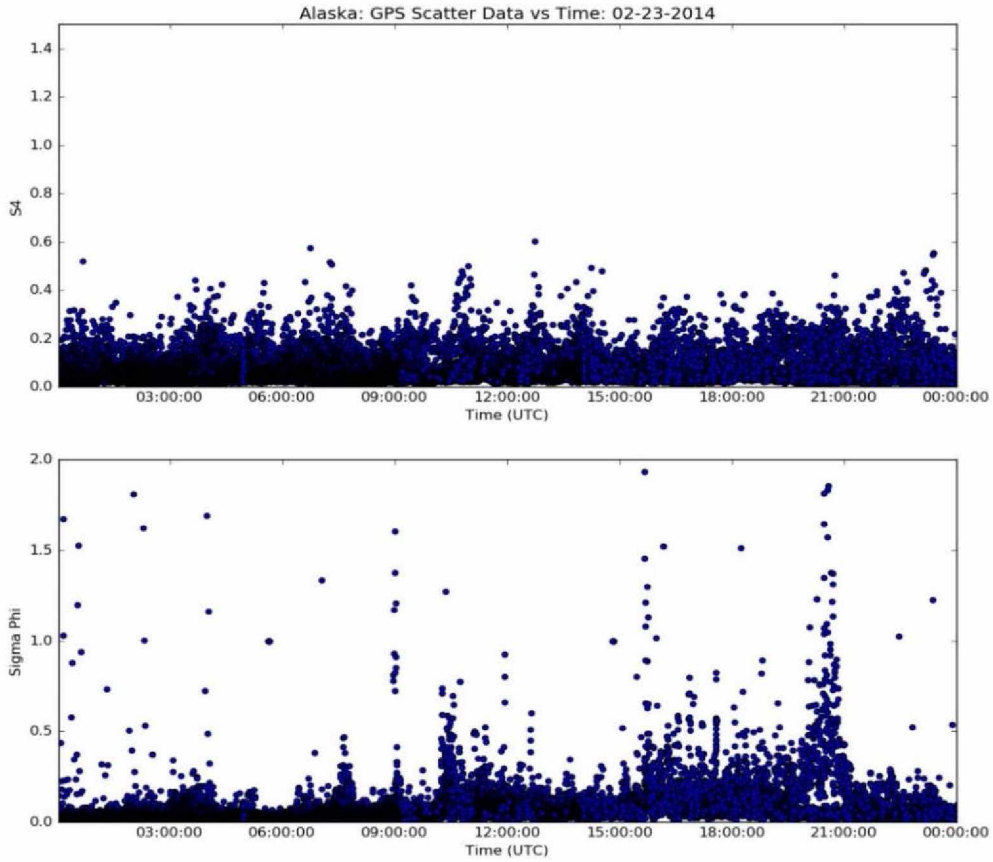

Figure 11: Scatter plot of time (UTC) vs GPS scintillation values for Alaska during 2/23/2014

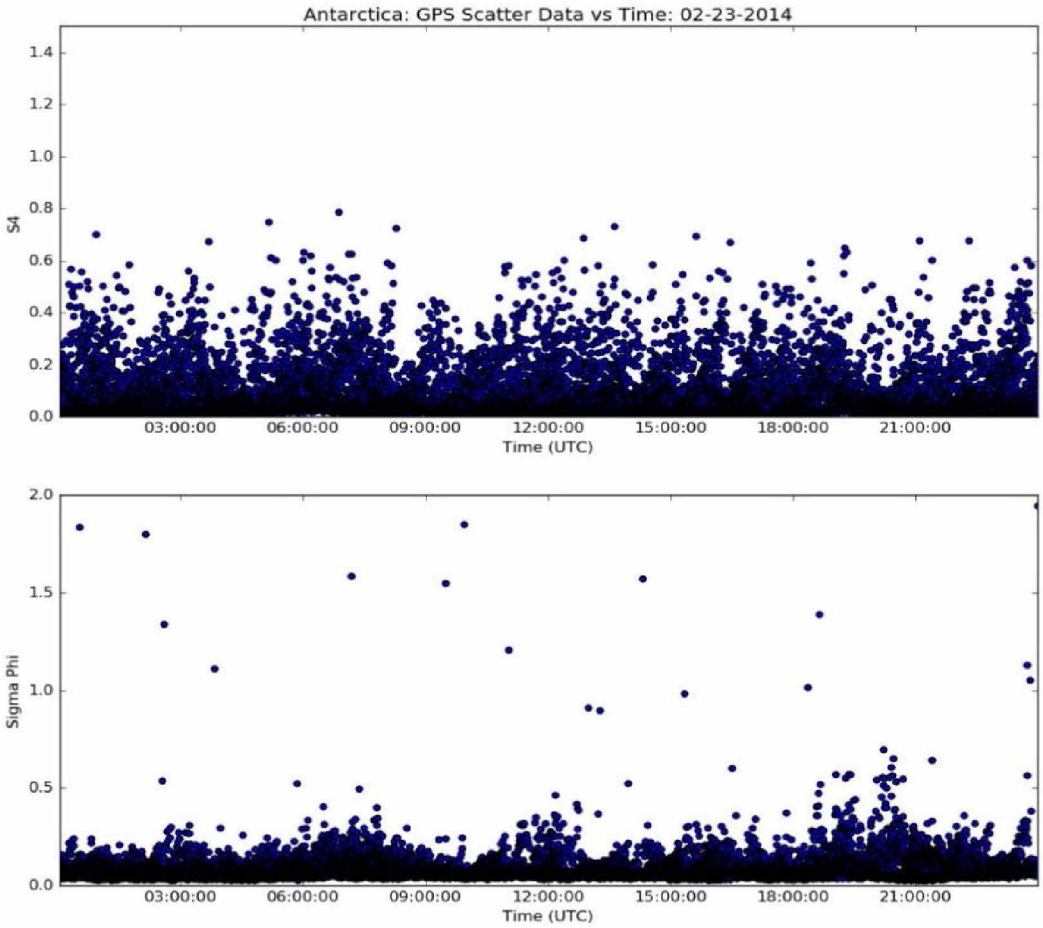

Figure 12: Scatter plot of time (UTC) vs GPS scintillation values for Antarctica during 2/23/2014

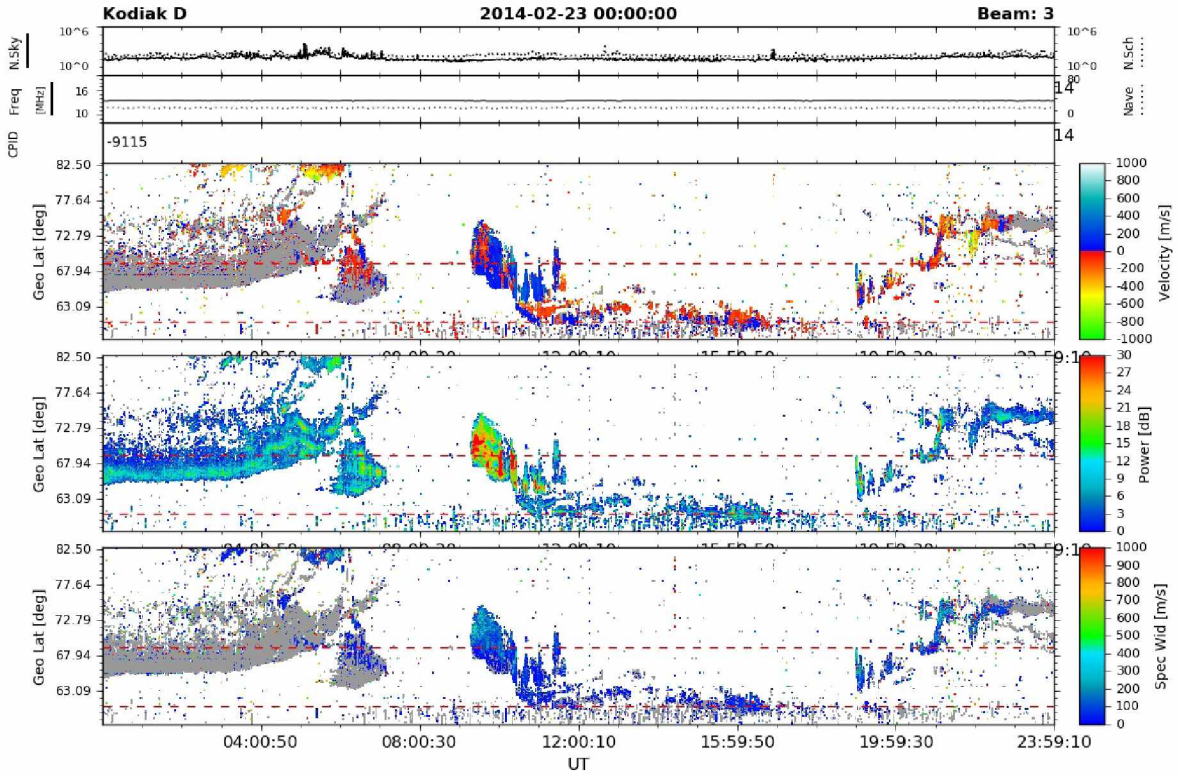

Figure 13: Kodiak SuperDARN taken for 2/23/2014 with the Poker Flat GPS field of view within the red lines

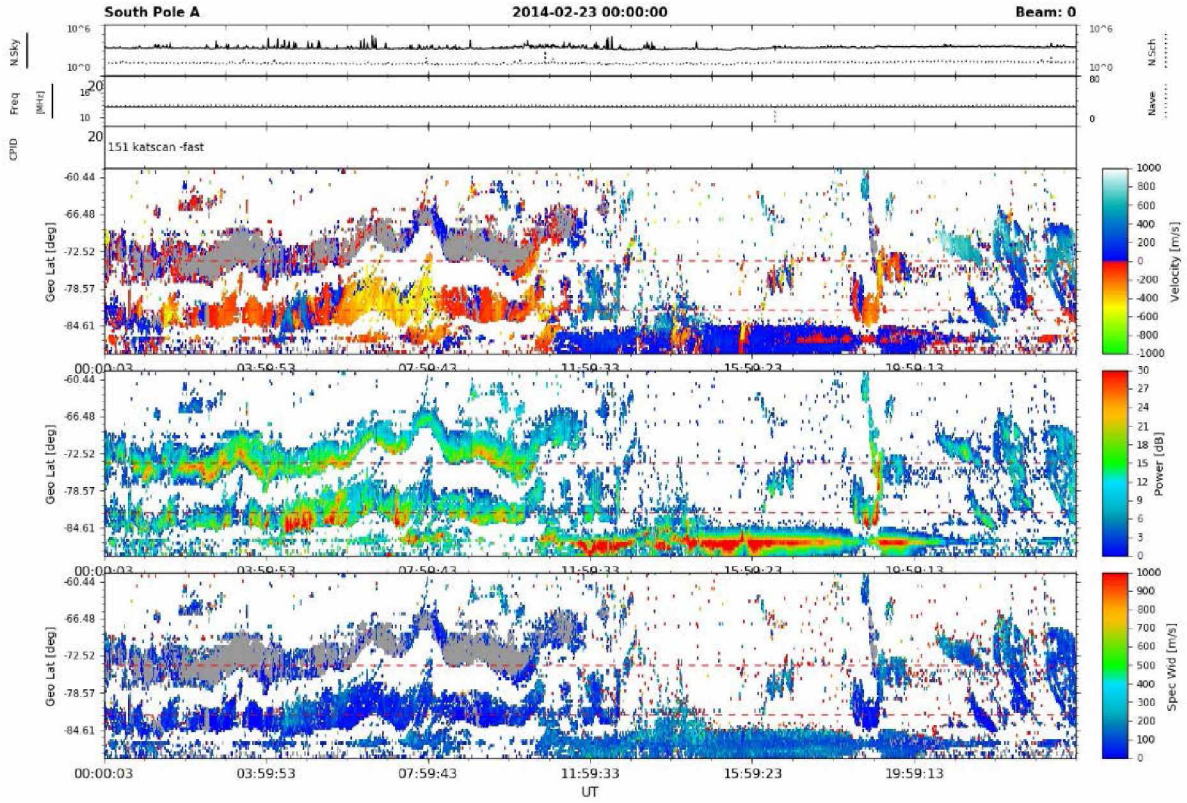

Figure 14: South Pole SuperDARN taken for 2/23/2014 with the McMurdo GPS field of view within the red lines

While it is clear from Figures 11 to 14 that there are periods of enhanced GPS scintillation without an obvious signature in the SuperDARN observations, further analysis is needed. The following examines a large database of scintillation observations and simultaneous SuperDARN observations to determine any statistically significant relationships.

Based on research by L. Spogli et al. [20] a threshold can be set to identify periods with moderate and strong scintillations. For their research, the threshold level needed to be of a certain value that would allow them to do an adequate statistical data analysis. They determined that a value of 0.25 was needed for both S_4 and σ_ϕ GPS values. For these reasons, this thesis also considered the value of 0.25 as the GPS threshold value. To confirm whether this threshold would select enough data for this study, histograms were created to analyze the scintillation values recorded during 2014 (see Figure 15 and Figure 16). Based on the histograms, it was decided that the 0.25 threshold does work for all locations. Approximately 1% of the S_4 and σ_ϕ measurements from the Alaskan data and the σ_ϕ measurement from the

Antarctica data fall above this 0.25 threshold, and about 7.3% of the Antarctic S_4 data fall above the threshold. Once the threshold was decided the data was compared against SuperDARN data matched by timestamp for each month.

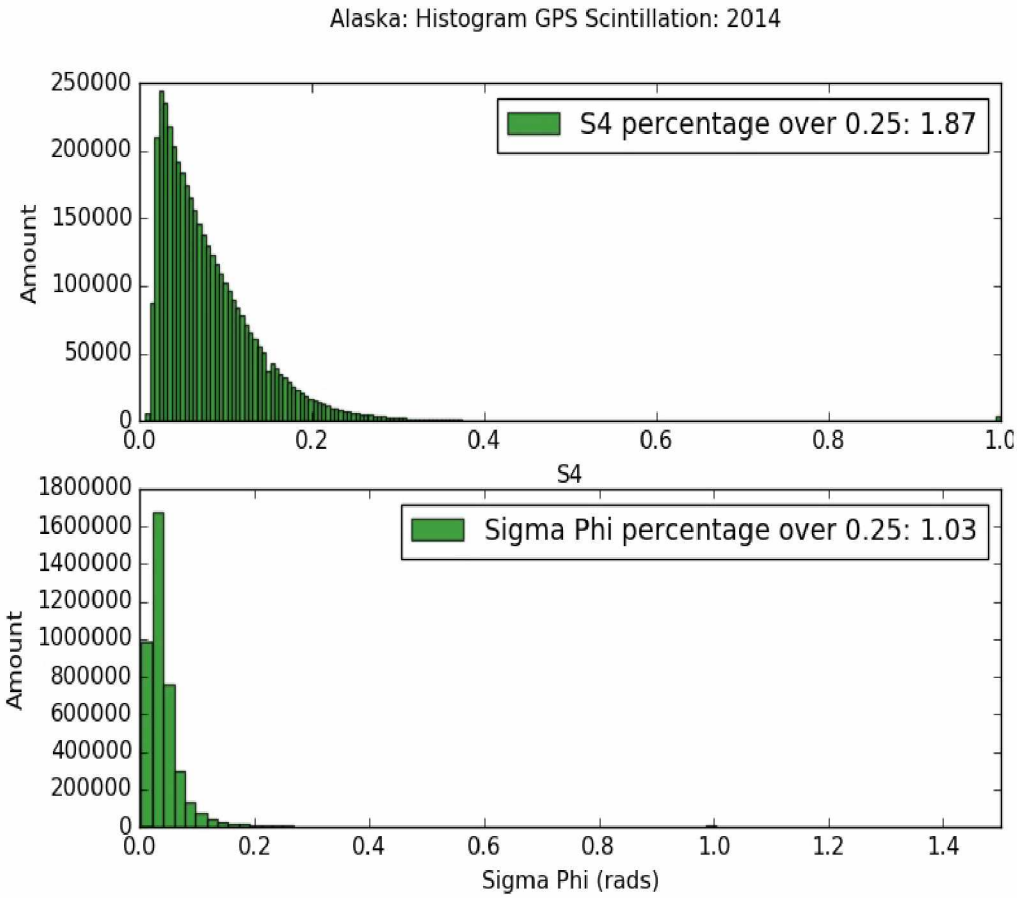

Figure 15: Histogram of Alaska data for 2014 indicating percentage of data over the set threshold

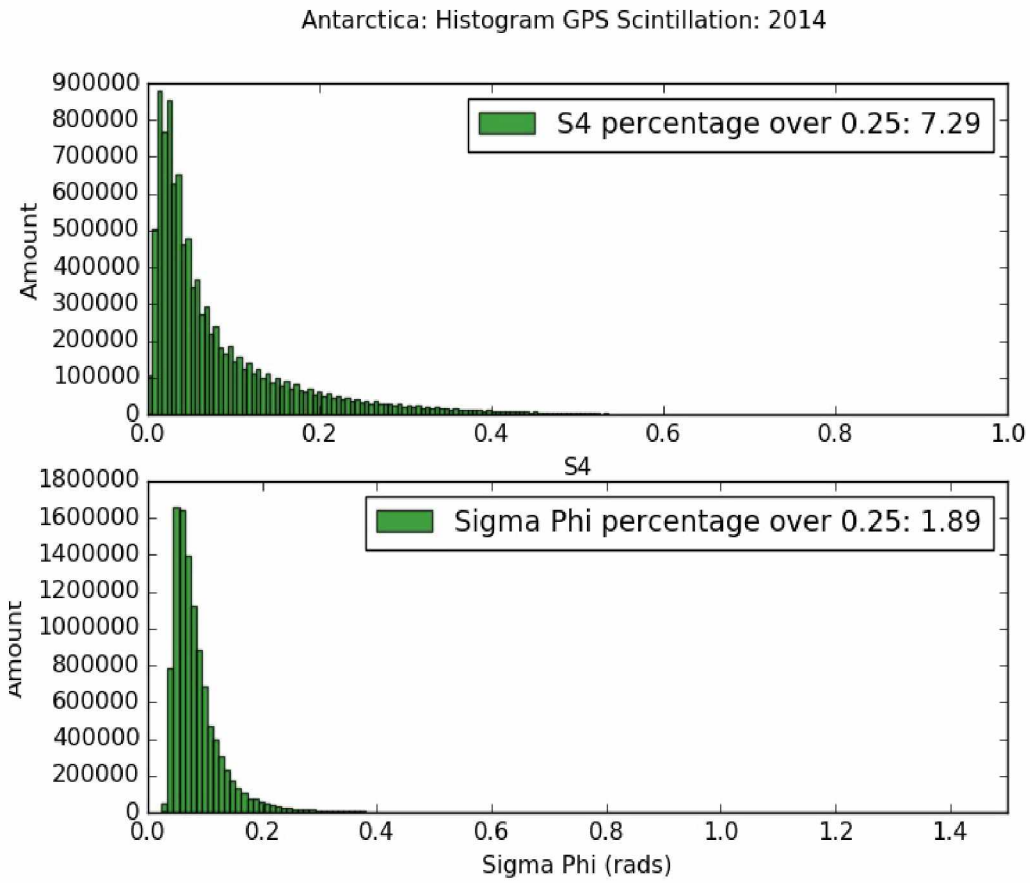

Figure 16: Histogram of Antarctica data for 2014 indicating percentage of data over the set threshold

Figure 17 tabulates the occurrence of scintillation versus the occurrence of radar scatter recorded by SuperDARN. Its purpose is to determine if there is a broad correspondence between scintillation and the occurrence of scatter. The figure shows a one-month total of measurements plotted versus local time. Solar-local-noon is indicated by the vertical yellow bar on each frame. The SuperDARN data were recorded as one-minute scans or as two-minute scans depending on the operating mode. The GPS data were matched to the closest minute recorded and analyzed to identify if any one data point in that minute had a value that was higher than the set thresholds. For each month the matched data was separated into four categories with an unknown amount of collectable data points. The amount of data is influenced by the varying number of days that data were collected per month, the amount of GPS pierce points per SuperDARN measurement, and SuperDARN's measurement rate. An example of this is shown in Figure 17, which shows Antarctica data collected during April 2013. During that month there were a total of 35,408 data points recorded during 25 out of the

possible 30 days. With Antarctica data, over 50% of the GPS station mask falls outside of the South Pole SuperDARN's field of view which greatly reduces the number of points that can be included. Analysis of the April data shows there were 28,168 time-matched data points that fell outside SuperDARN's field of view. Therefore, there were 7,240 valid matched data points. If these data points were evenly spread over 24 hours, the hourly rate of observations for the month of April would have been 301 total valid data points per hour divided among the categories.

The top left bar graph in Figure 17 is denoted as 'No Scintillation Recorded – No SuperDARN recorded' (NSR-NSD). To fit the NSR-NSD requirement, S_4 or σ_ϕ values must be below the scintillation threshold and concurrently no SuperDARN data that fell underneath the required criteria. The second bar graph (top right) is denoted as 'Scintillation Recorded – No SuperDARN recorded' (SR-NSD). For the SR-NSD bar plot, the recorded S_4 or σ_ϕ values must be above the threshold, and no concurrent SuperDARN data that fit the criteria were recorded in the neighborhood of the ionospheric pierce points. The third bar graph (bottom left) is denoted as 'No Scintillation Recorded – SuperDARN recorded' (NSR-SD) and indicates when there was SuperDARN data recorded that fit the criteria and the concurrent S_4 or σ_ϕ values were below the threshold. The fourth bar plot (bottom right) is denoted as the 'Scintillation Recorded-SuperDARN recorded' (SR-SD) and indicates when there was both SuperDARN data that fit the criteria and S_4 or σ_ϕ values that were above the threshold for that timestamp.

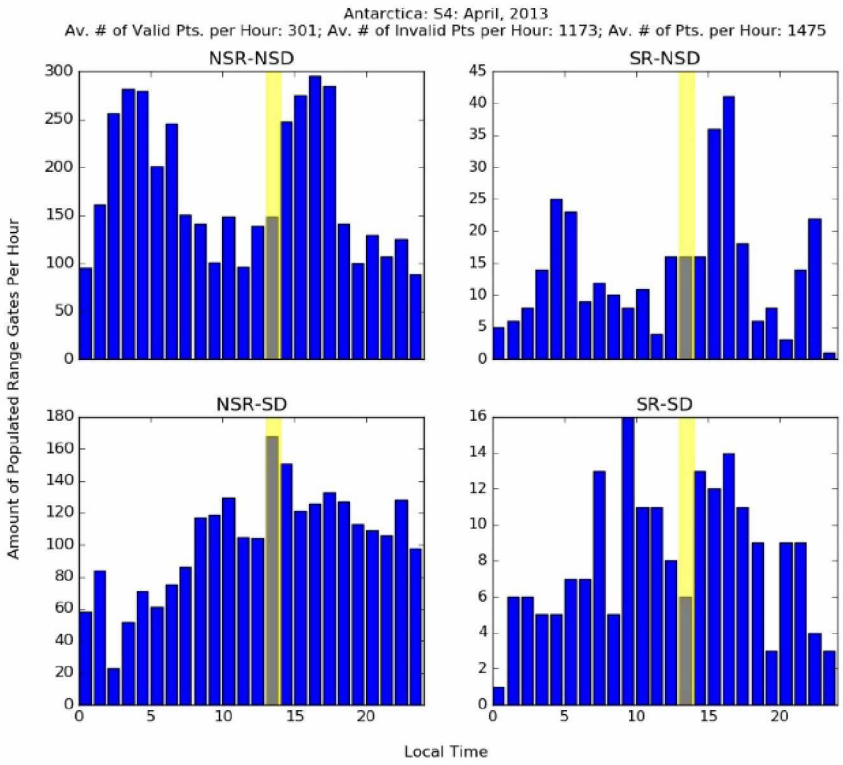

Figure 17: A bar plot of April 2013 showing different amounts of data seen at different hours throughout the month

When comparing all four y-axis values the NSR-NSD peaks are always the highest of the four categories, with values in the 100 to 500 range. The values with the next highest peaks are on the NSR-SD's bar plots. It can also be noted that SR-NSD peaks are normally larger than SR-SD peaks. Since there are values in the SR-SD bar plot, these values indicate that when there is GPS scintillation recorded, a portion of this scintillation is also recorded by SuperDARN. The large difference between NSR-SD and SR-NSD values indicates that there are many irregularities that are identified by SuperDARN. However, these small-scale irregularities may not be related to the large-scale irregularities that directly cause interference with GPS signals. To see if there were any trends in regards to scintillation occurrences during a certain time frame or time period, the SR-SD data was further analyzed. The largest peaks in SR-SD data can be found when analyzing the data based on the S_4 variable.

Each month of the study period (December 2013-November 2015) was analyzed in the same format as Figure 17. There are a total of 17 months of Alaska data that can be evaluated. During these months, the data indicates that the highest percentage of occurrence of scintillation is the time frame between 20:00 - 23:00 local time (see Figure 18). This peak

occurred in 82% of the S_4 data analyzed. There is a lower percentage within the σ_ϕ data at 53%. There do not seem to be any related seasonal or solar weather patterns within either group of months.

There are a total of 23 months of Antarctica data that can be evaluated. During these months, the data also indicated that the highest percentage of occurrence is the same as the Alaska data and is between 20:00 – 23:00 local time (see Figure 19). This peak occurred in 57% of the S_4 data analyzed. σ_ϕ data, however, did not achieve the 50% level, with the highest level measured at 48%. There do not seem to be any related seasonal or solar weather patterns within either group of months.

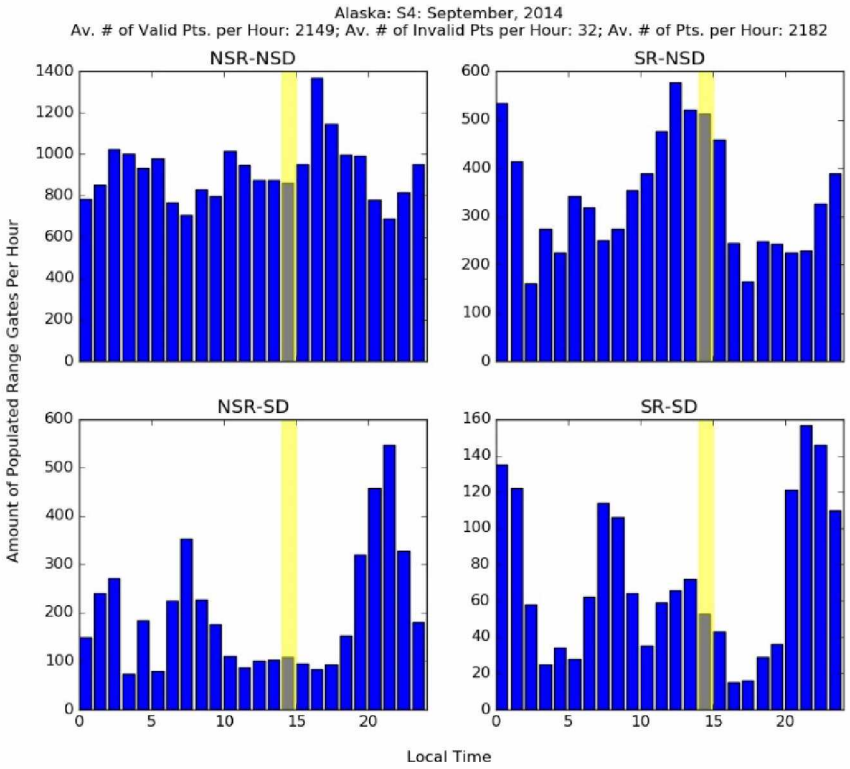

Figure 18: Alaska S_4 bar graph for September, 2014 demonstrating the spike peak between 20:00 - 23:00 local time

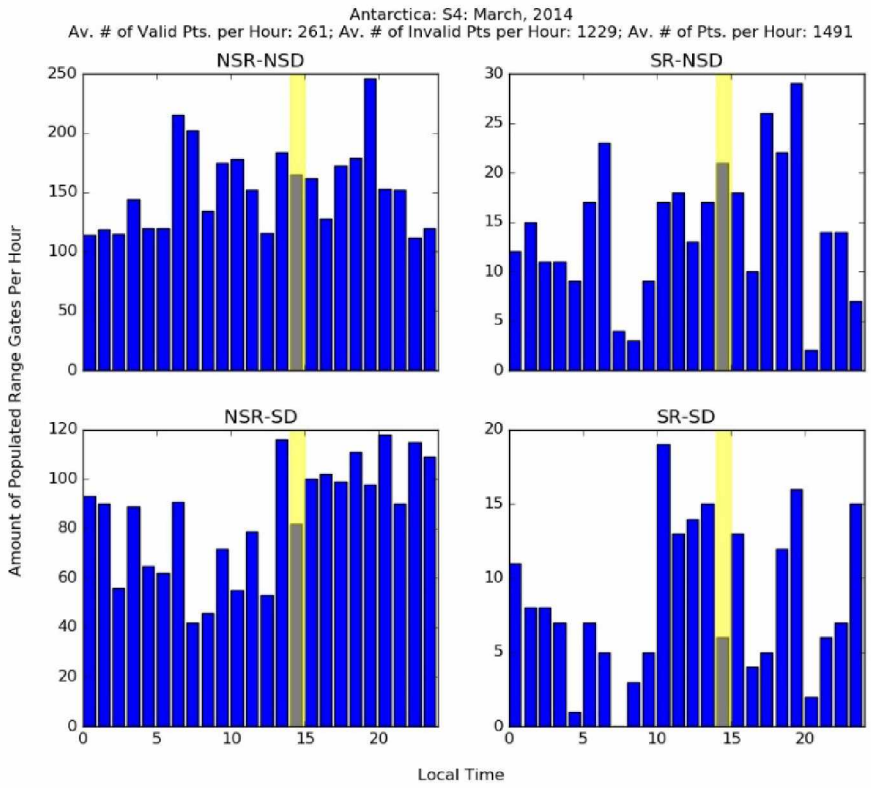

Figure 19: Antarctica S_4 bar graph for March, 2014 demonstrating the spike peak between 20:00 - 23:00 local time

3.7 Monthly SuperDARN Radar Returned Values vs S_4 or σ_ϕ GPS Scintillation Values Scatter Plots

In this section, the data are presented as scatter and contour plots. These plots were intended to identify possible patterns between SuperDARN radar signal parameters and GPS scintillation values, with each plot graphed over one month of observations. Both types of GPS scintillation values are plotted versus the SuperDARN radar received power, velocity, and spectral width. In these plots an average of the GPS scatter is matched to the average SuperDARN parameter within the neighborhood of the ionospheric pierce point.

For each location, both S_4 and σ_ϕ scatter plots show that most of the data points fell underneath the accepted scintillation threshold. This is expected, as the threshold was set to capture only about 1% to 2% of the observations (see Figure 20 and Figure 21). Each of the plots show a line indicating a fit to the mean (purple) of the points averaged over bins of each parameter. Both locations showed similar data plots with no conclusive evidence of any patterns. Although no pattern is indicated, the data and the plotted lines were examined further to confirm this initial observation.

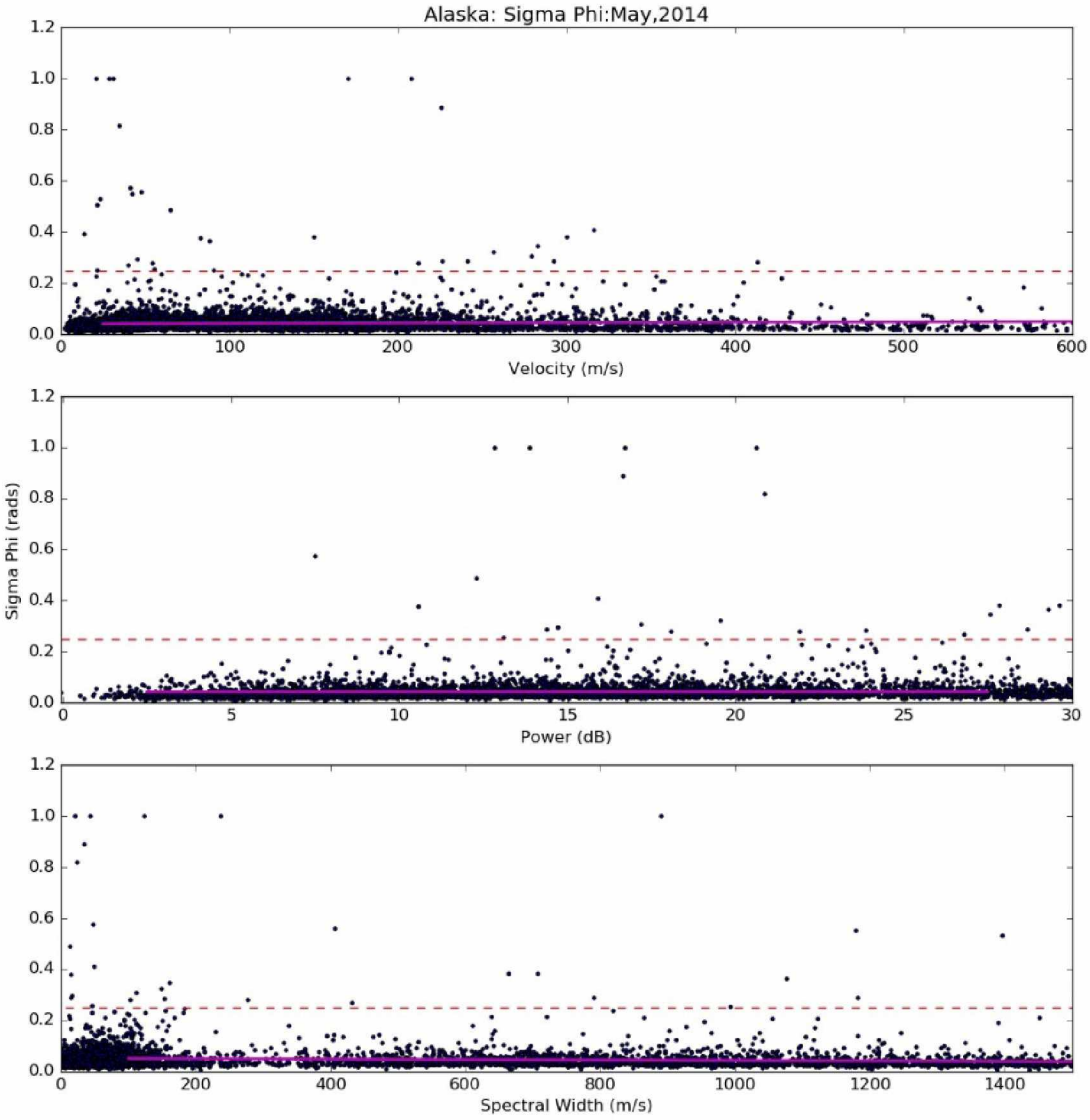

Figure 20: A May, 2014 scatter plot of the Alaska data

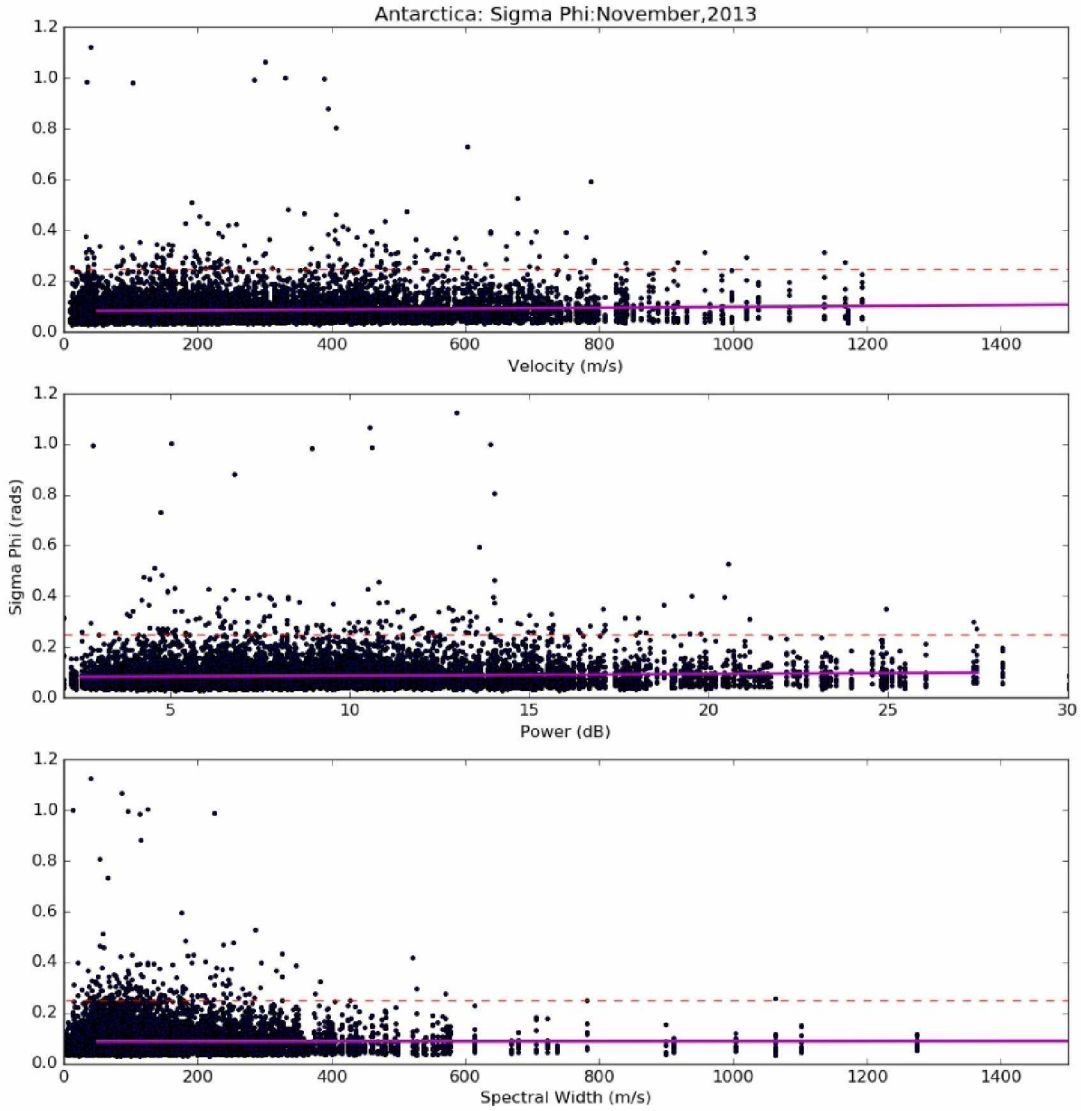

Figure 21: A November, 2013 scatter plot of the Antarctica data

To further examine the data behind these scatter plots (Figure 20 and Figure 21), histograms were created for scintillation data falling within ranges of the SuperDARN parameters. For each histogram the GPS scintillation values were broken into separate groups based on the matching SuperDARN radar values range. Each group of data was then further analyzed by calculating the average (blue) and standard deviation (red) and plotting them as dashed vertical lines. This was done as another means to find trends in the observations. The histograms demonstrated that the low GPS scintillation values exist at a majority of the ranges of the SuperDARN values, and there were not significant changes of the distributions with increasing parameter values. Within the histograms for Alaska, the two GPS scintillation values

demonstrated different distribution patterns. The S_4 histograms appear Gaussian in distribution for every SuperDARN value, while the σ_ϕ histograms appear more like a Rayleigh distribution (see Figure 22 - Figure 27). Within the histograms for Antarctica, all plots show a Rayleigh distribution for both σ_ϕ and S_4 (see Figure 28 - Figure 33).

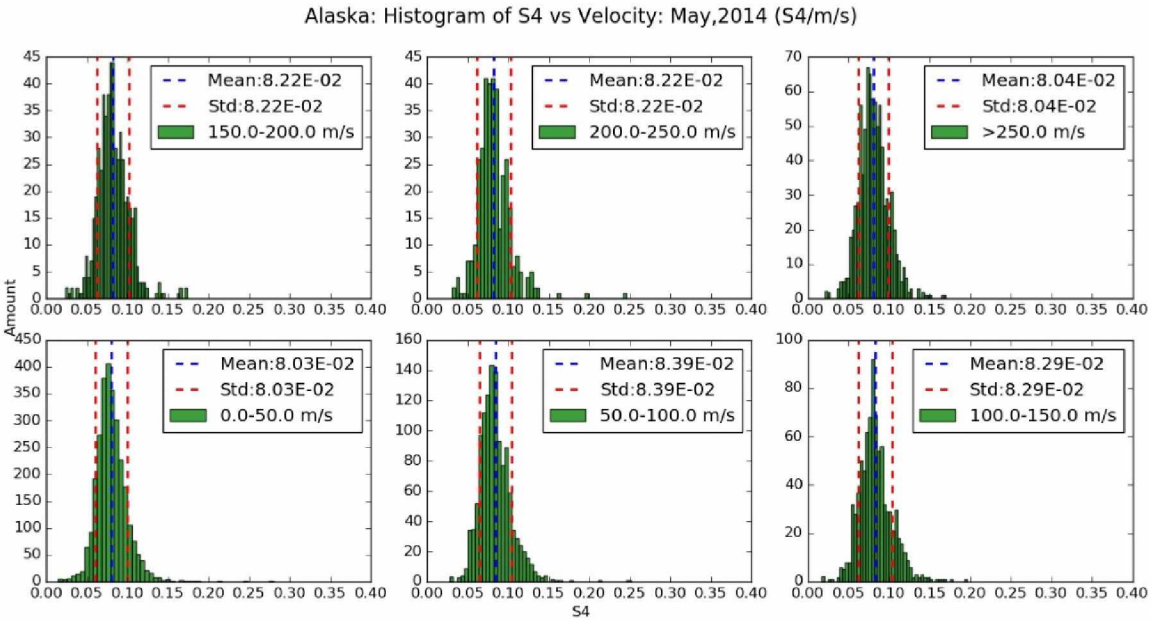

Figure 22: An Alaska histogram of S_4 vs velocity for May, 2014

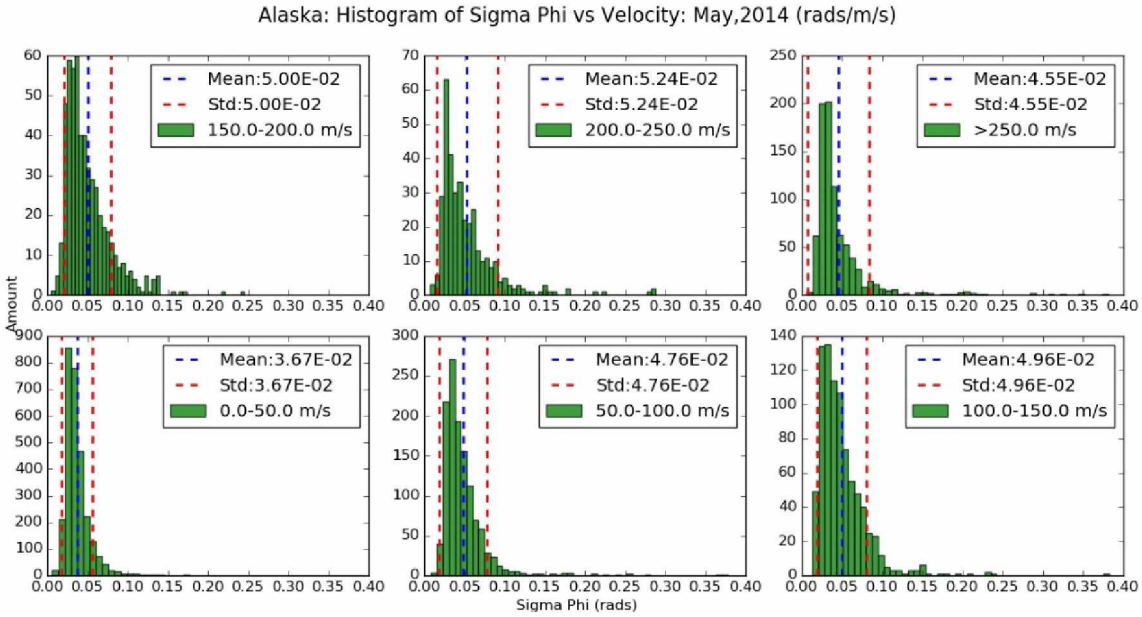

Figure 23: An Alaska histogram of σ_φ vs velocity for May, 2014

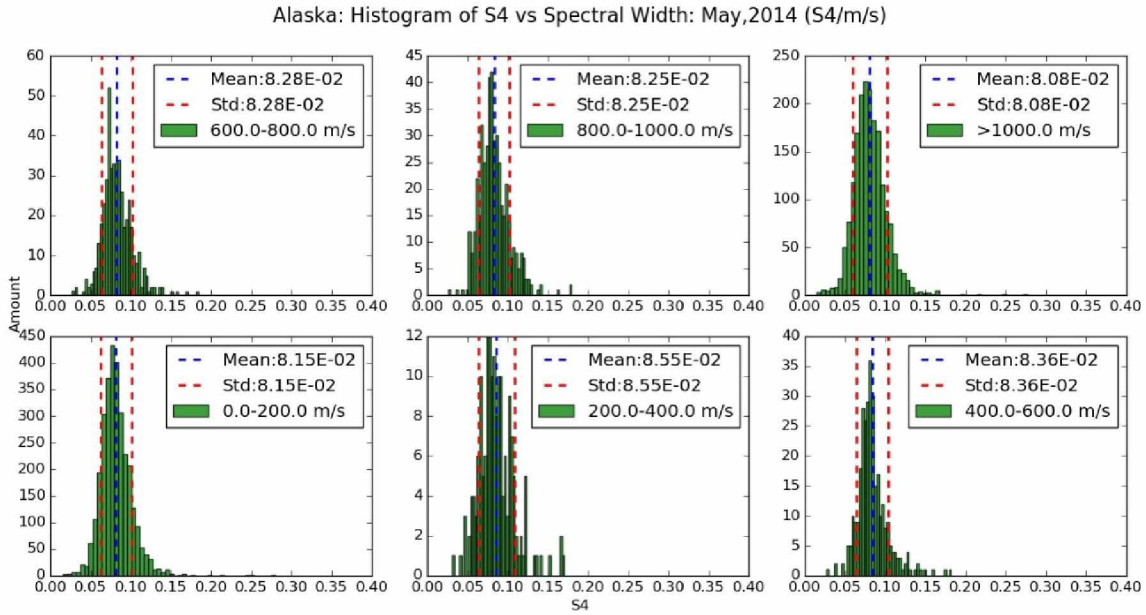

Figure 24: An Alaska histogram of S_4 vs spectral width for May, 2014

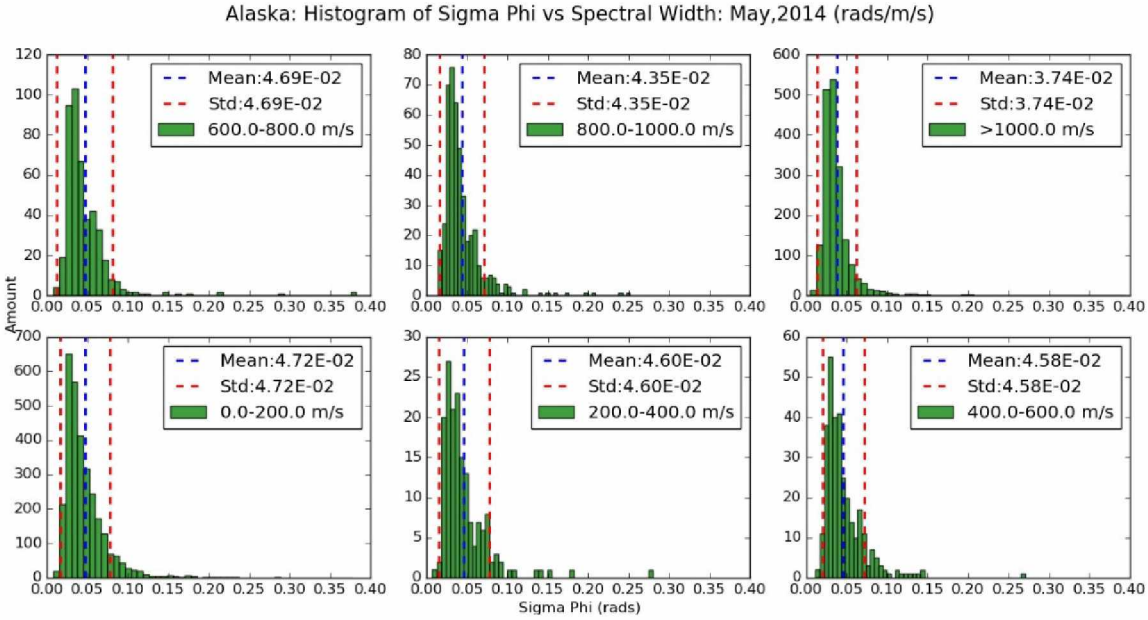

Figure 25: An Alaska histogram of σ_φ vs spectral width for May, 2014

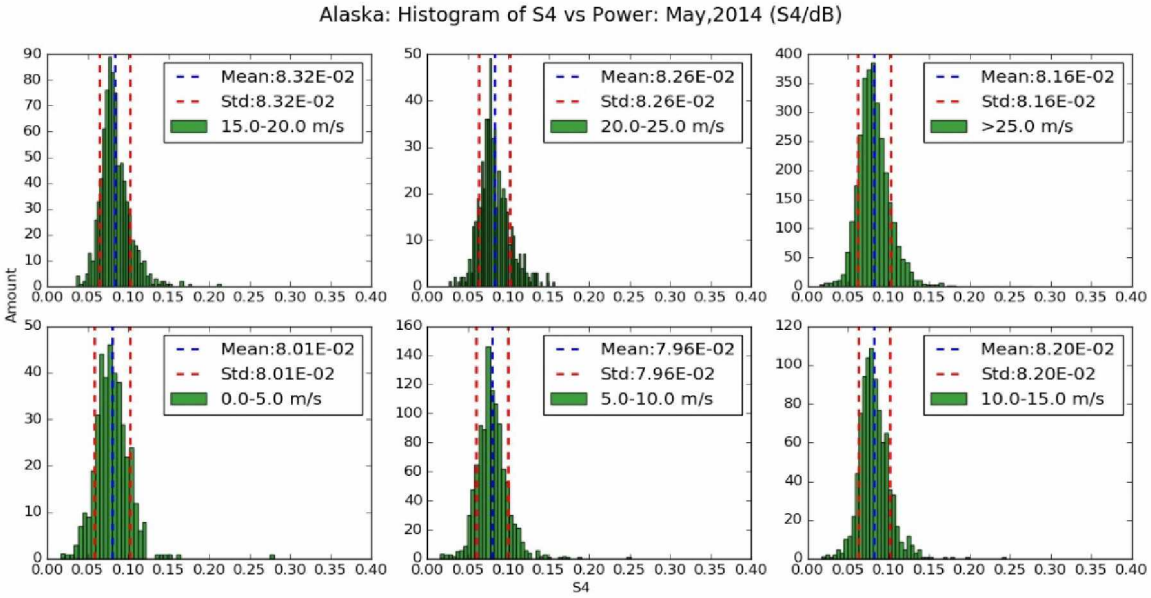

Figure 26: An Alaska histogram of S_4 vs power for May, 2014

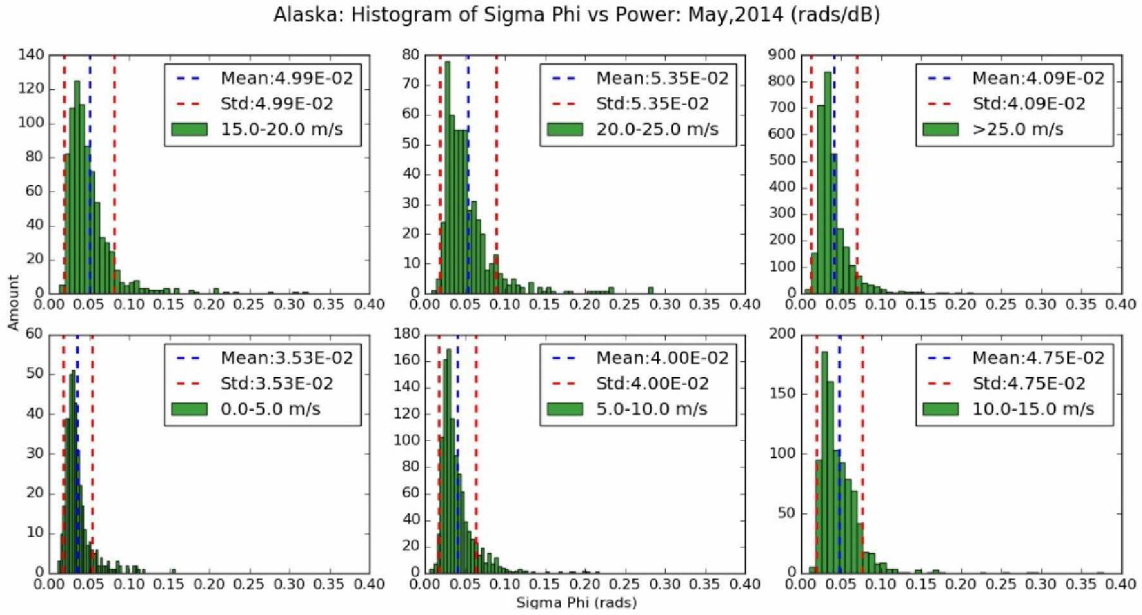

Figure 27: An Alaska histogram of σ_φ vs power for May, 2014

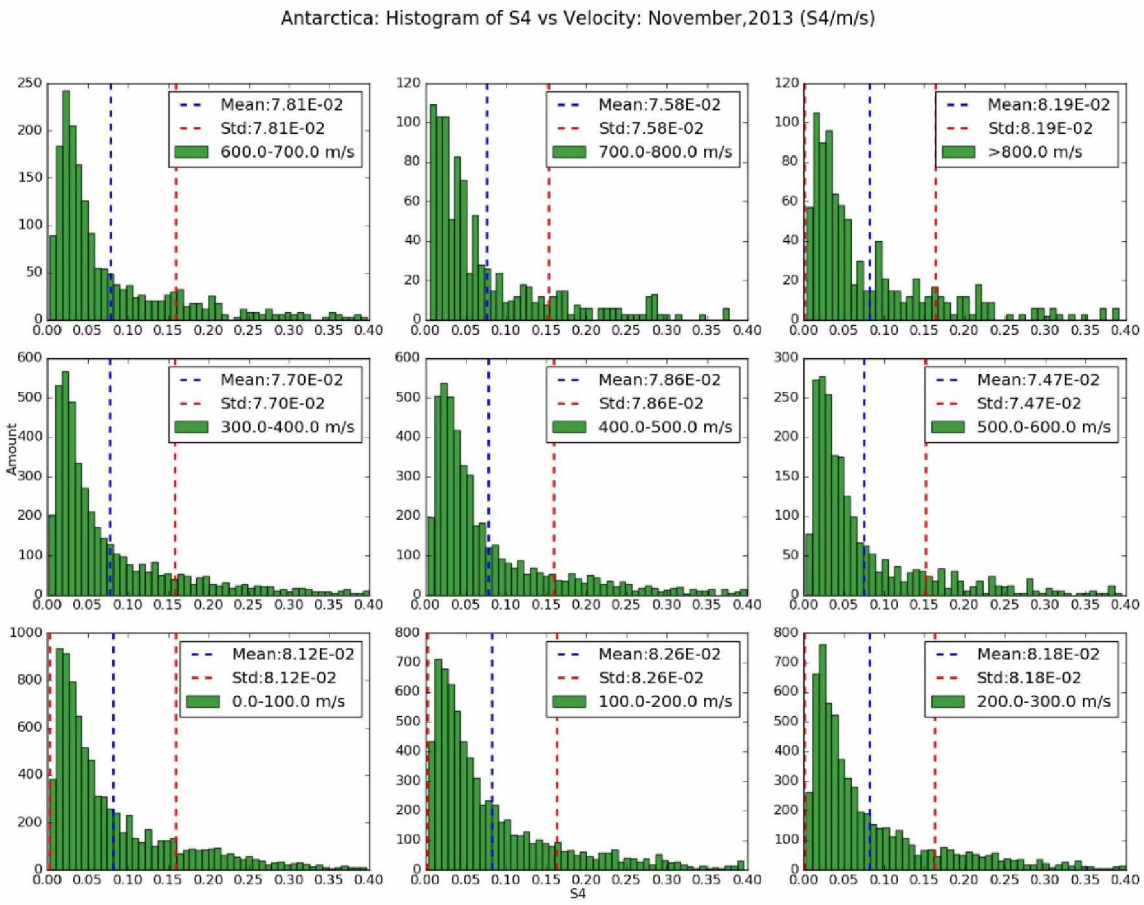

Figure 28: An Antarctica histogram of S_4 vs velocity for November 2013

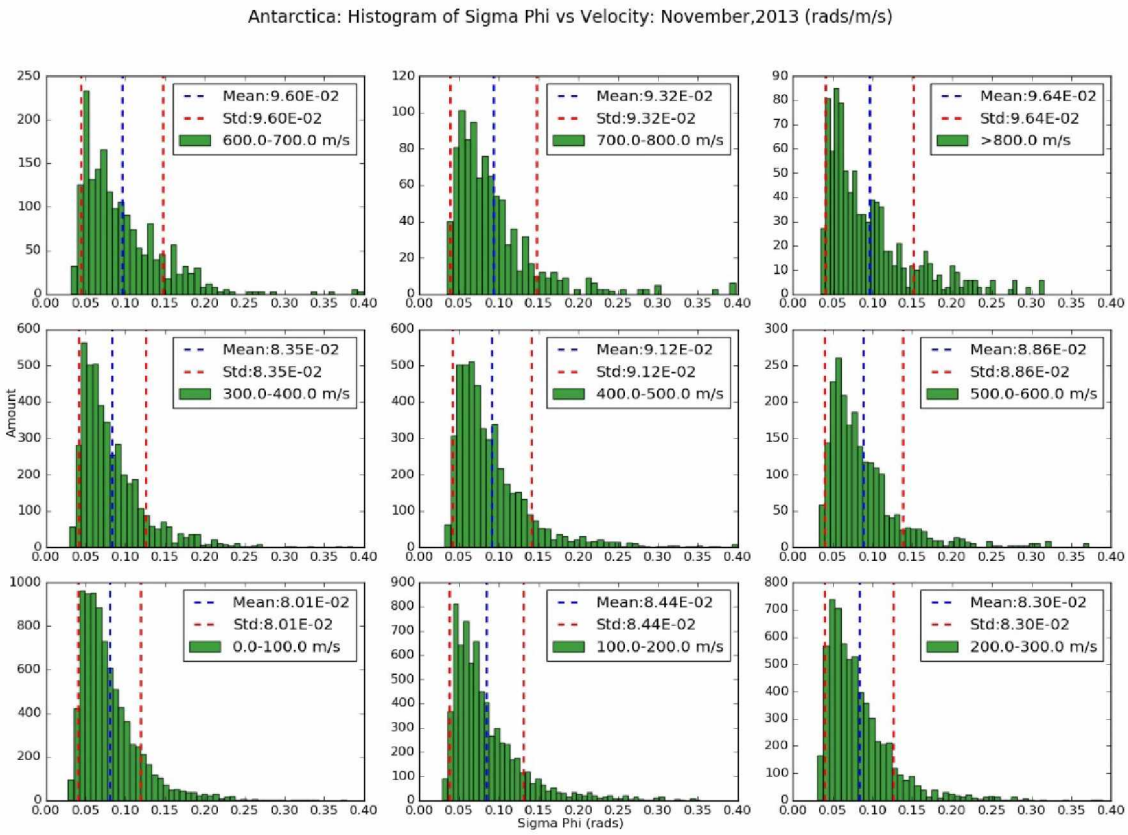

Figure 29: An Antarctica histogram of σ_φ vs velocity for November 2013

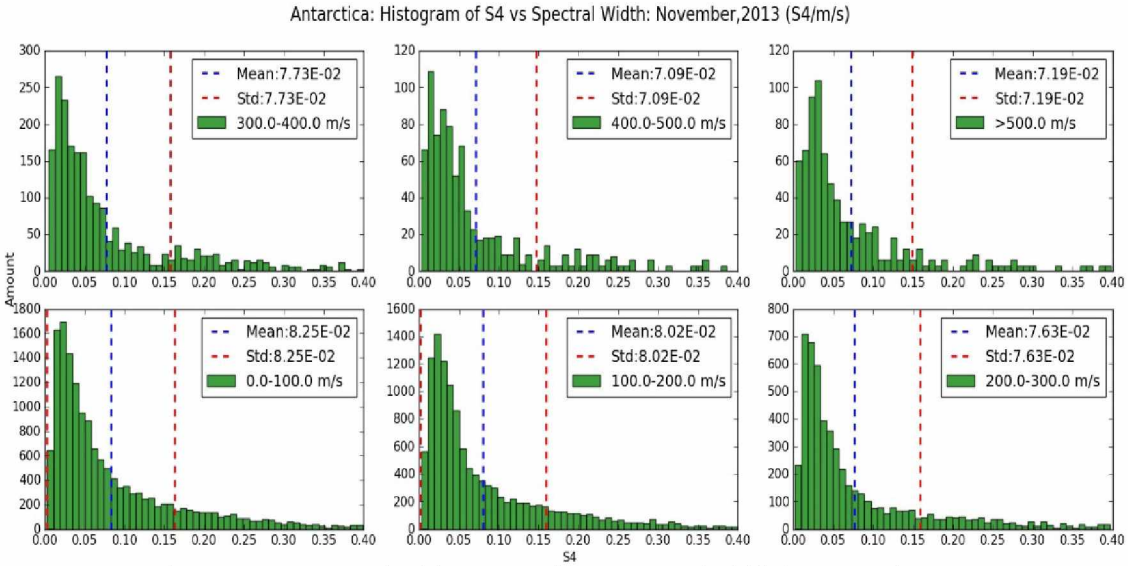

Figure 30: An Antarctica histogram of S_4 vs spectral width for November 2013

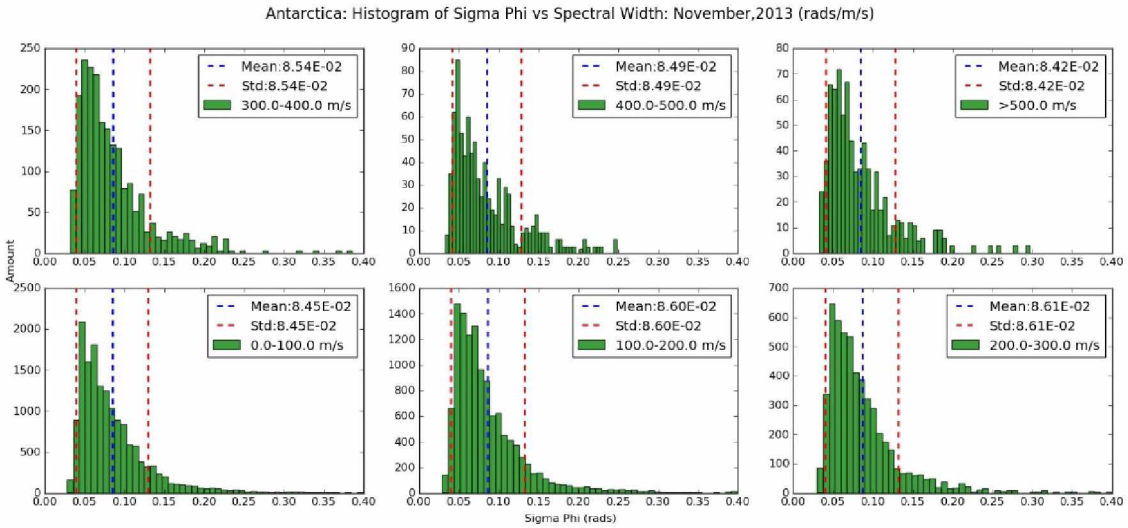

Figure 31: An Antarctica histogram of σ_φ vs spectral width for November 2013

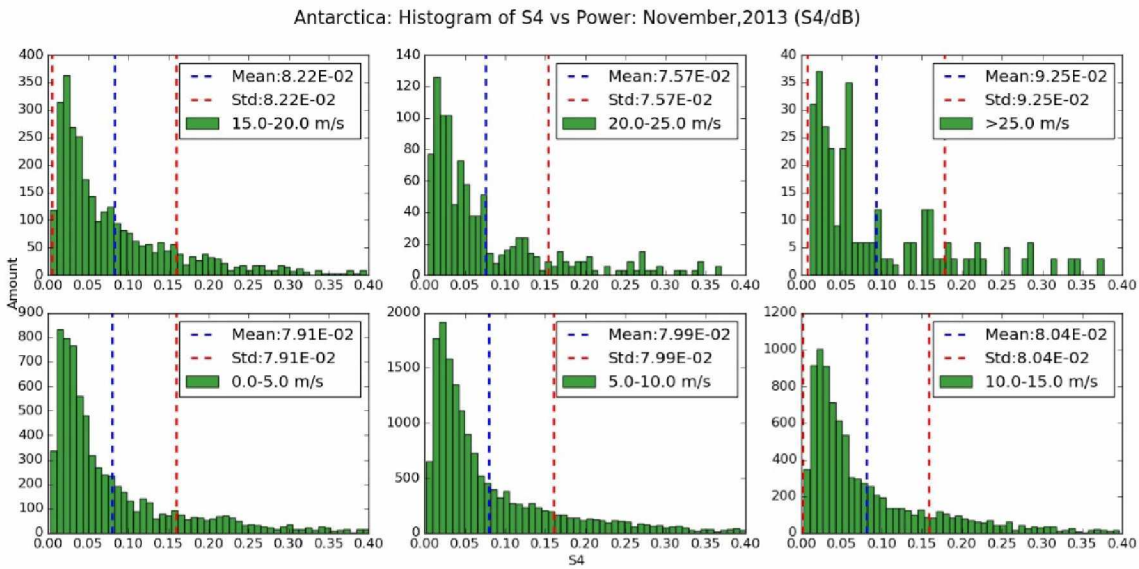

Figure 32: An Antarctica histogram of S_4 vs power for November 2013

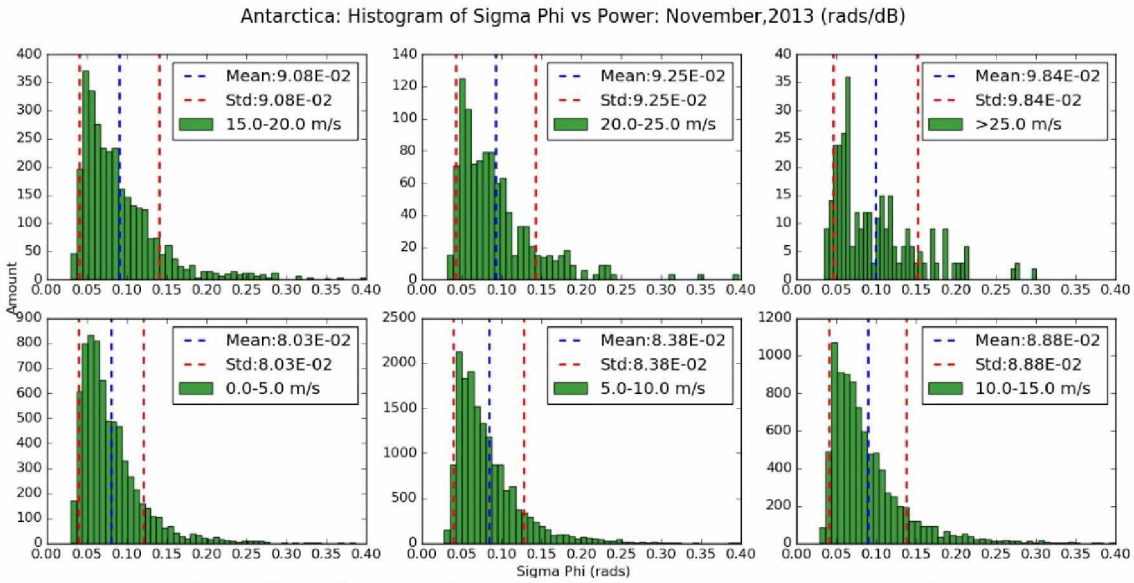

Figure 33: An Antarctica histogram of σ_φ vs power vs for November 2013

Since the data points shown on both scatter plots are so densely packed it is difficult to determine trends. To help remedy this, contour plots of the scatter data were generated (see Figure 34 and Figure 35). The lines showing fits to the mean and mode of the binned data were redrawn on these plots.

When the SuperDARN radar return values are plotted as contour plots (see Figure 34 and Figure 35), the data still displays little evidence that either S_4 or σ_ϕ have a strong dependence on the SuperDARN signal parameters. Each frame of the figures shows the slopes of the fit lines that were found based on the average calculated for each bin was shown in the histogram. In determining the fits, the uncertainty of the mean factored in as the error to help correct for outliers. Both locations show slopes that are in essence horizontal. This demonstrates that GPS scintillation value can occur for any SuperDARN value.

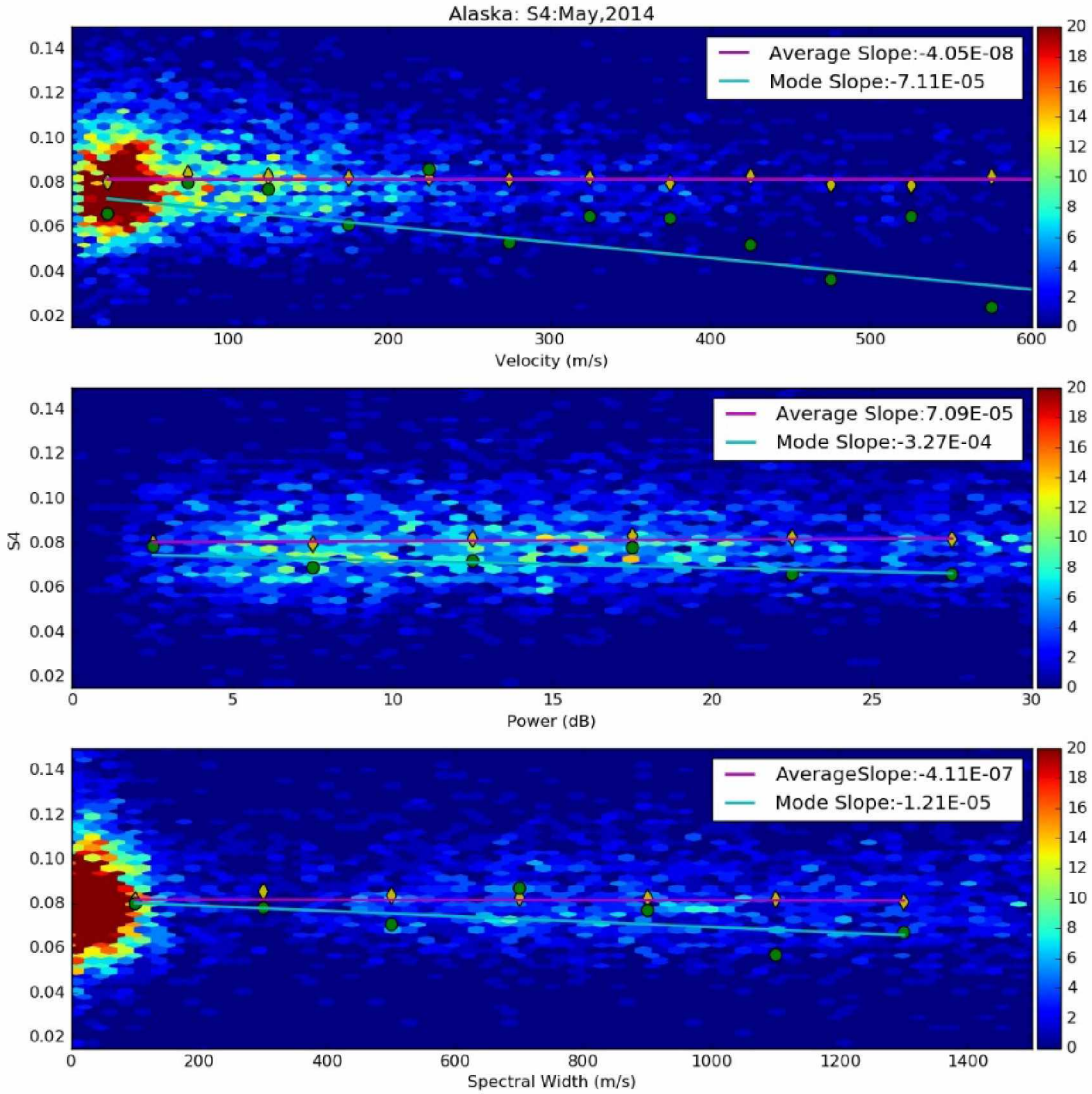

Figure 34: An Alaskan data contour plot of May, 2014 S_4 data

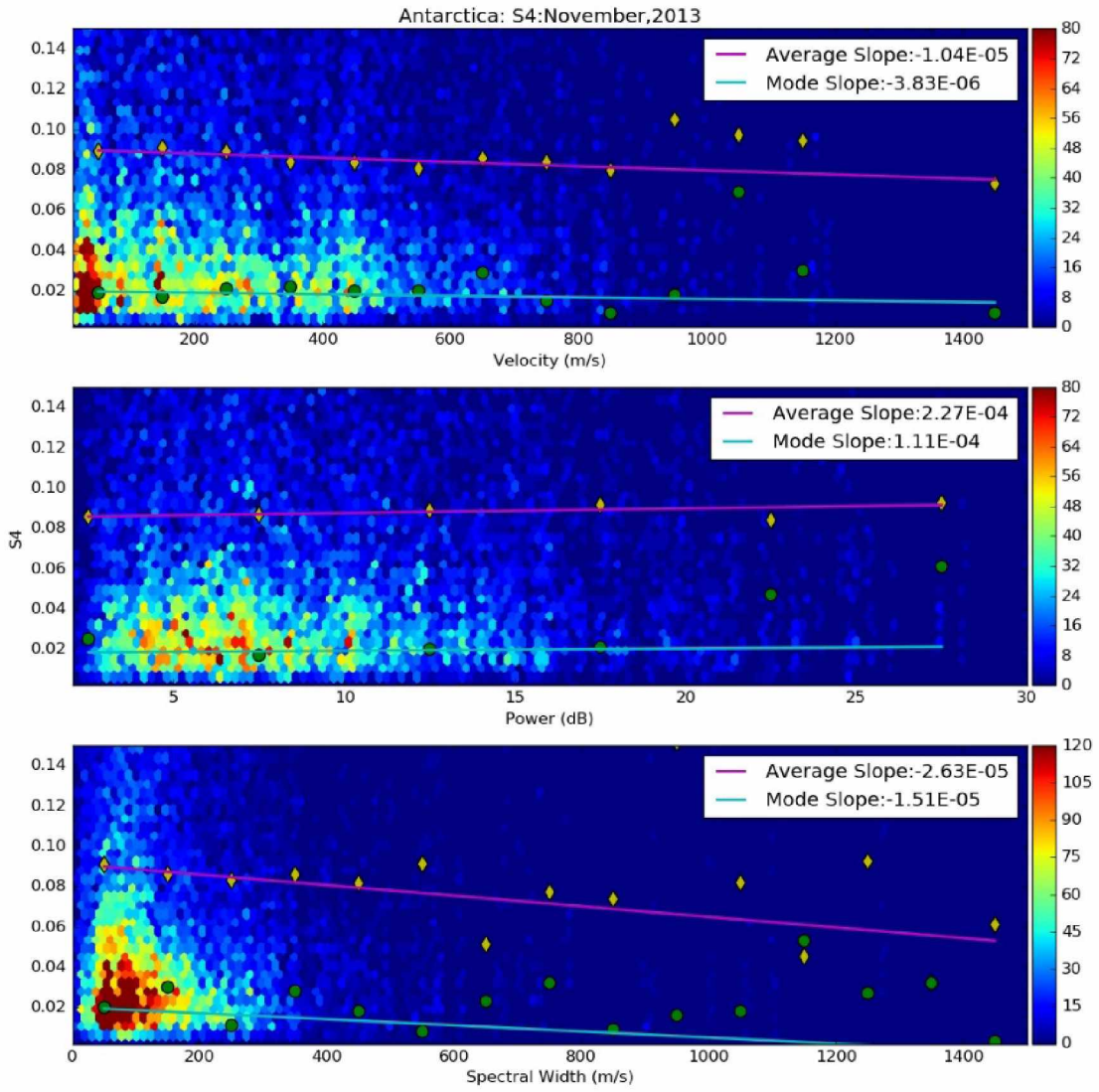

Figure 35: An Antarctica data contour plot of November, 2013 S_4 data

3.8 Regression Coefficient Plots

The average slope demonstrated in Figure 34 and Figure 35 along with the uncertainty of the calculated slope for each month over a single year were calculated and then plotted as a bar graph (see Figure 36 - Figure 47). Each bar in the graph refers to the corresponding month's average regression coefficient. It should be noted that due to the lack of data, there is a 0 value recorded within the Alaska plots during the months of July and December 2014. Also, by using the uncertainty of the calculated mean from each mean GPS point the uncertainty of the slope was found and plotted on the graph as well.

By examining these graphs for each location it can be seen that most of these plots demonstrate that large fluctuations occur from month to month (see Figure 36 - Figure 47). Analyzing the Alaska data shows that the minimum regression coefficients occur predominantly during the summer. For Antarctica, the majority of the plots demonstrate periods of lower regression coefficients during April and August when Antarctica is shifting to and from full twilight. If there are peaks within the bar plots they tend to be between October through February. Otherwise, no other trends appear to be evident.

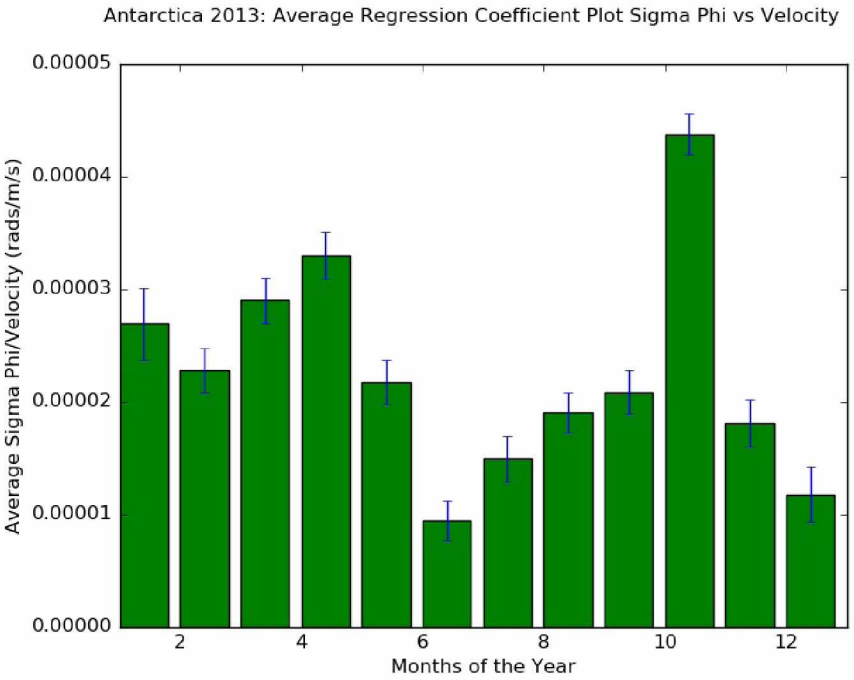

Figure 36: Alaska average regression coefficient plot σ_φ vs Velocity for 2014

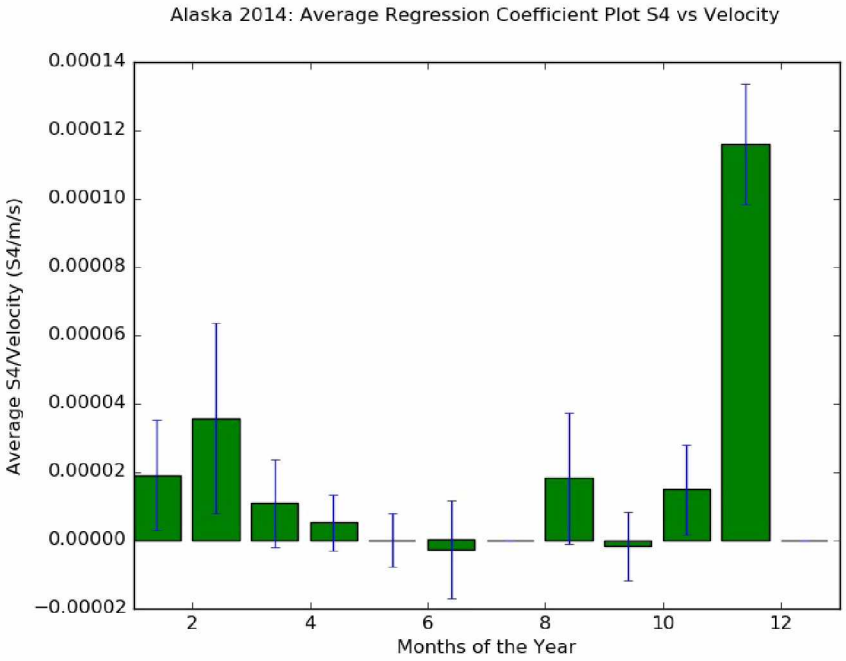

Figure 37: Alaska average regression coefficient plot S_4 vs Velocity for 2014

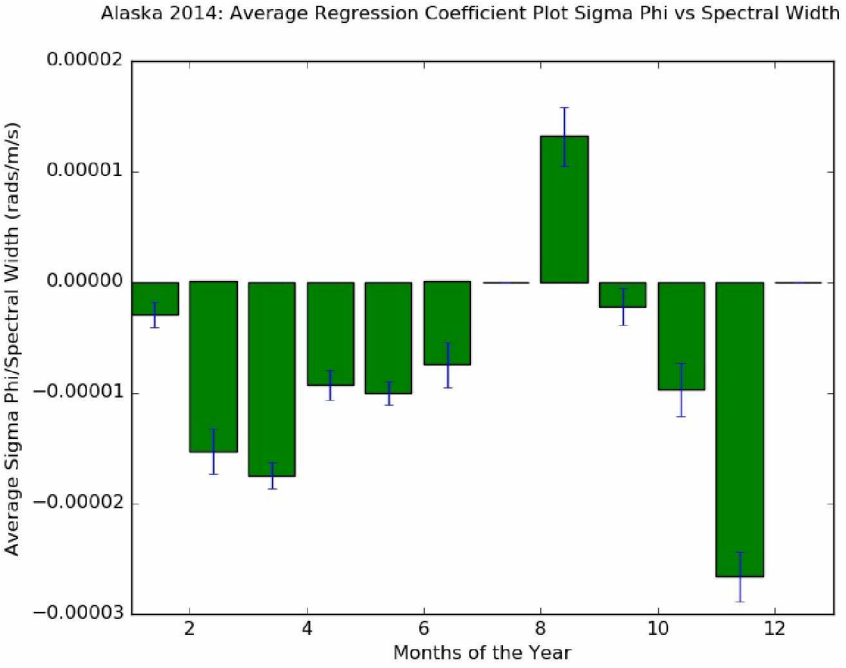

Figure 38: Alaska average regression coefficient plot σ_φ vs Spectral Width for 2014

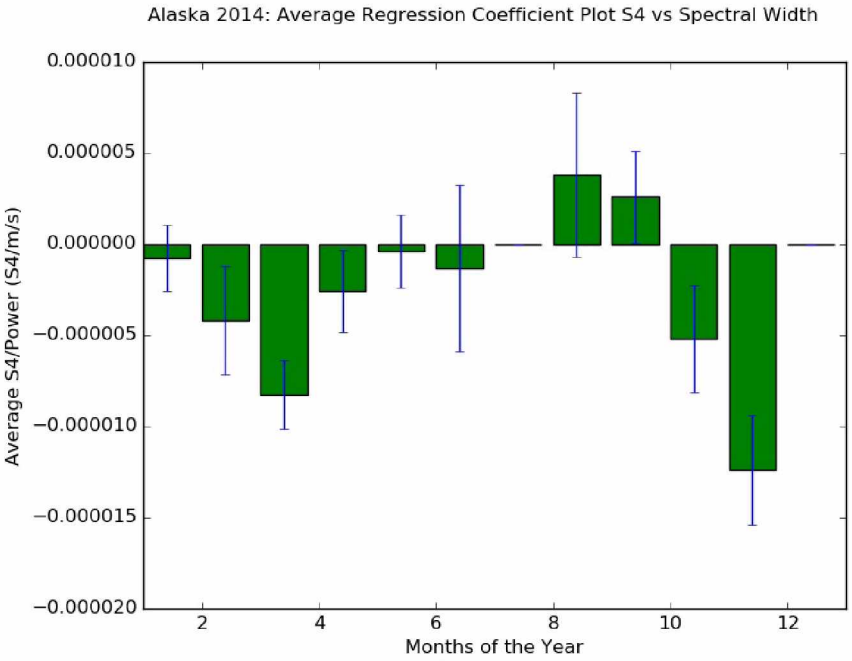

Figure 39: Alaska average regression coefficient plot S_4 vs Spectral Width for 2014

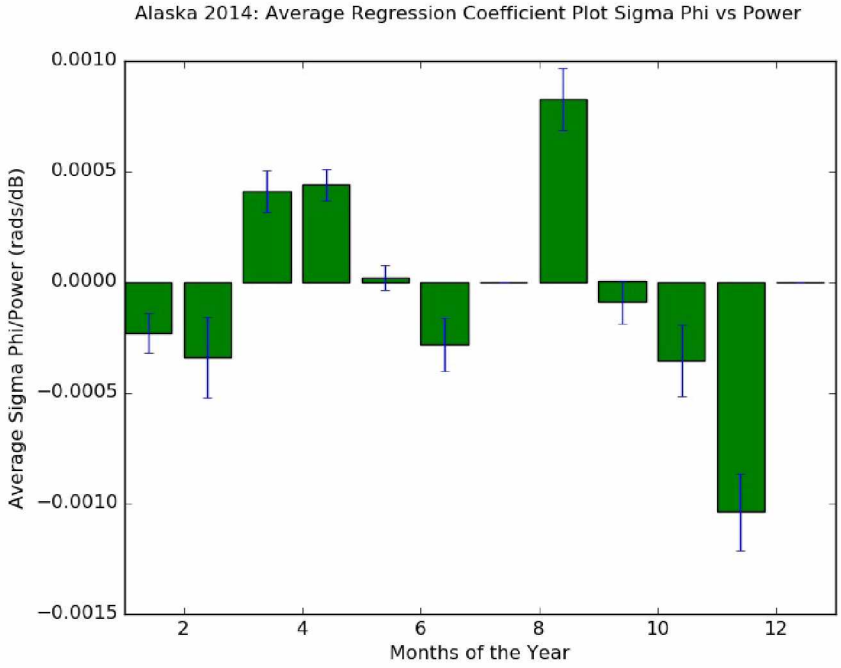

Figure 40: Alaska average regression coefficient plot σ_φ vs Power for 2014

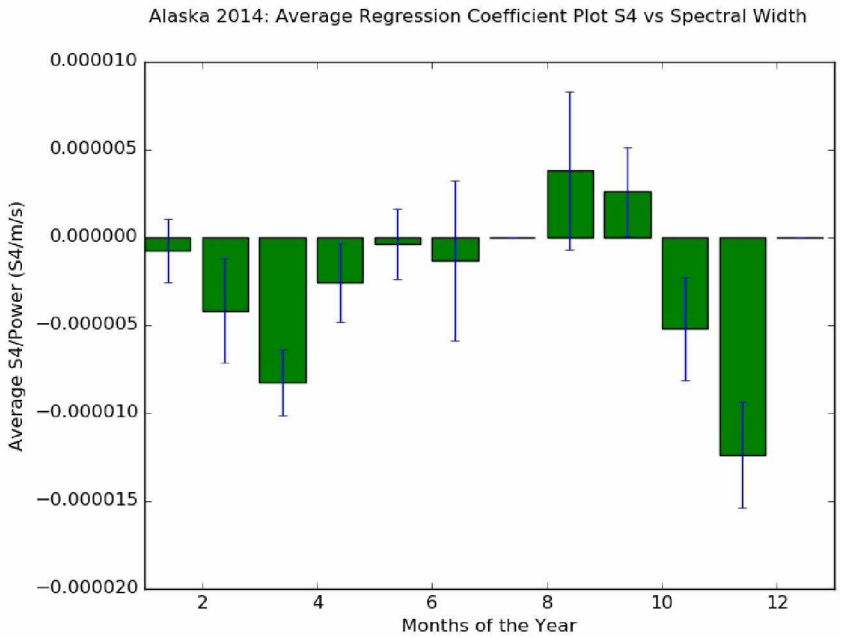

Figure 41: Alaska average regression coefficient plot S_4 vs Power for 2014

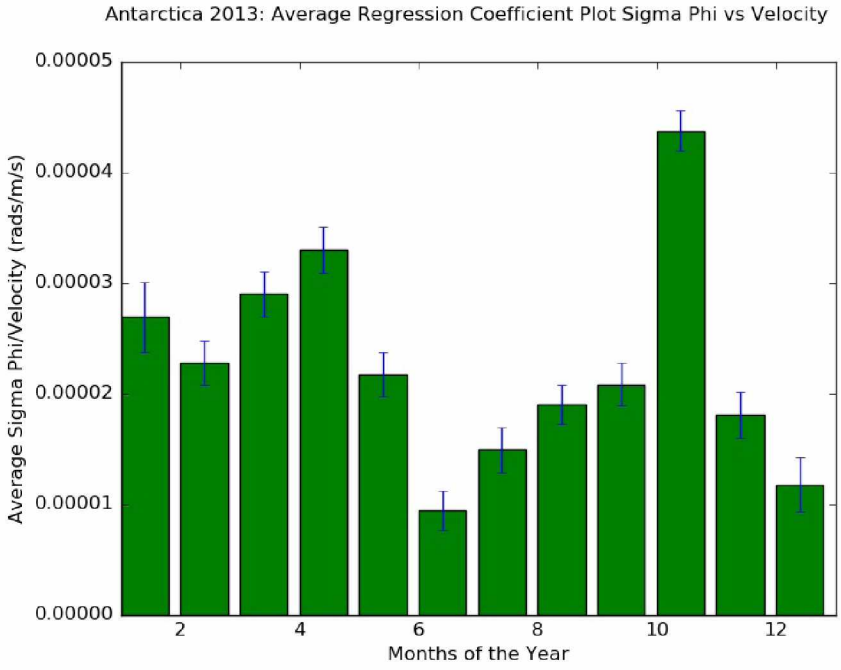

Figure 42: Antarctica average regression coefficient plot σ_φ vs Velocity for 2013

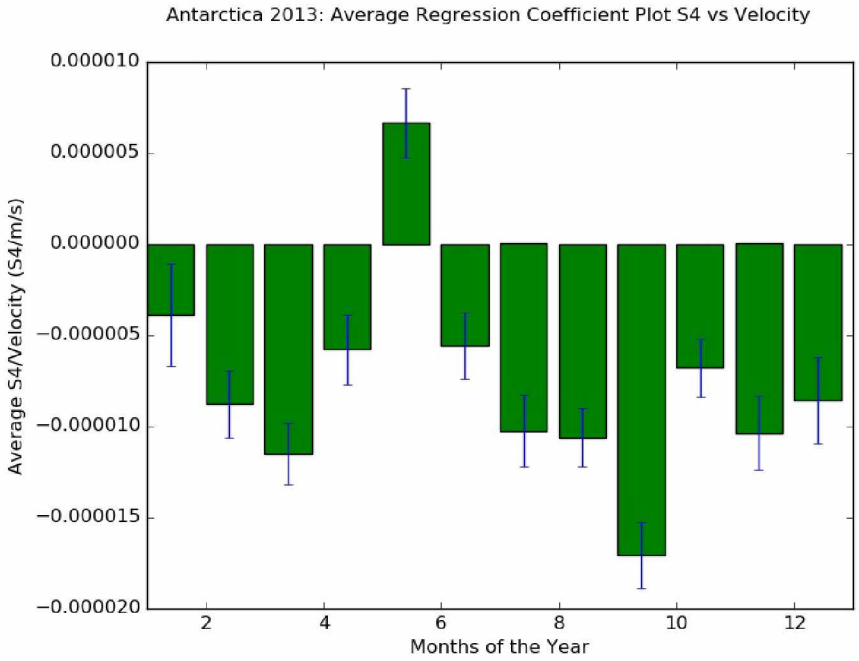

Figure 43: Antarctica average regression coefficient plot S_4 vs Velocity for 2013

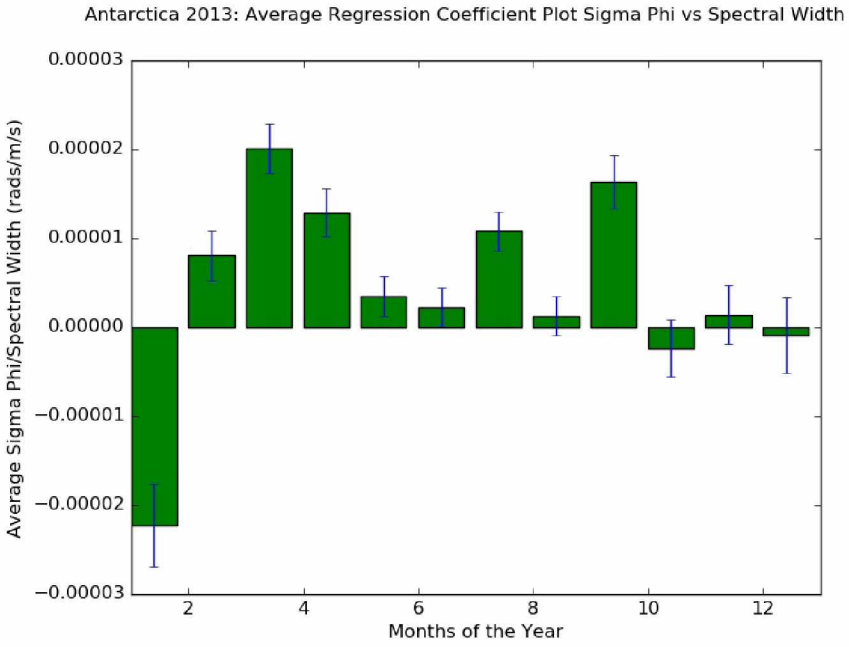

Figure 44: Antarctica average regression coefficient plot σ_φ vs Spectral Width for 2013

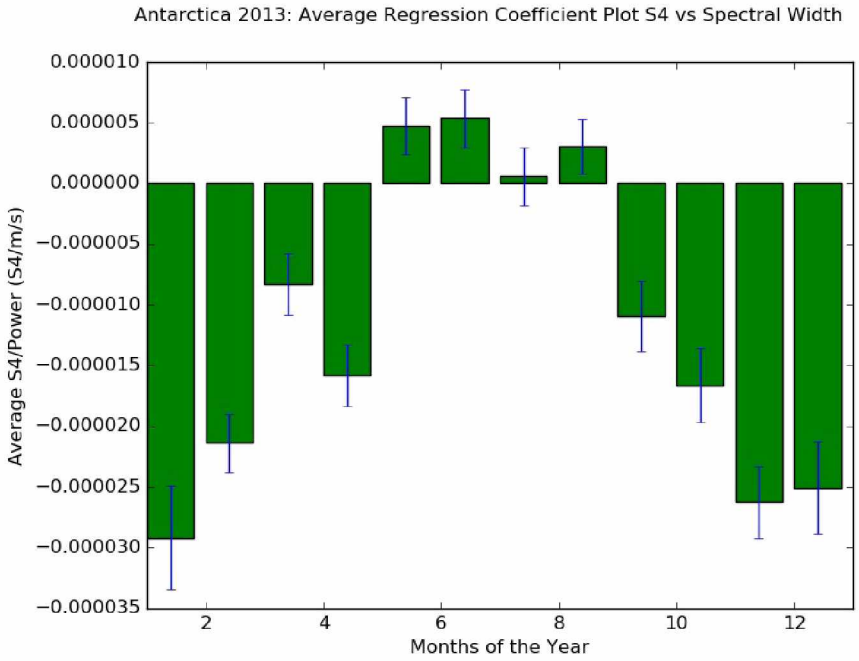

Figure 45: Antarctica average regression coefficient plot S_4 vs Spectral Width for 2013

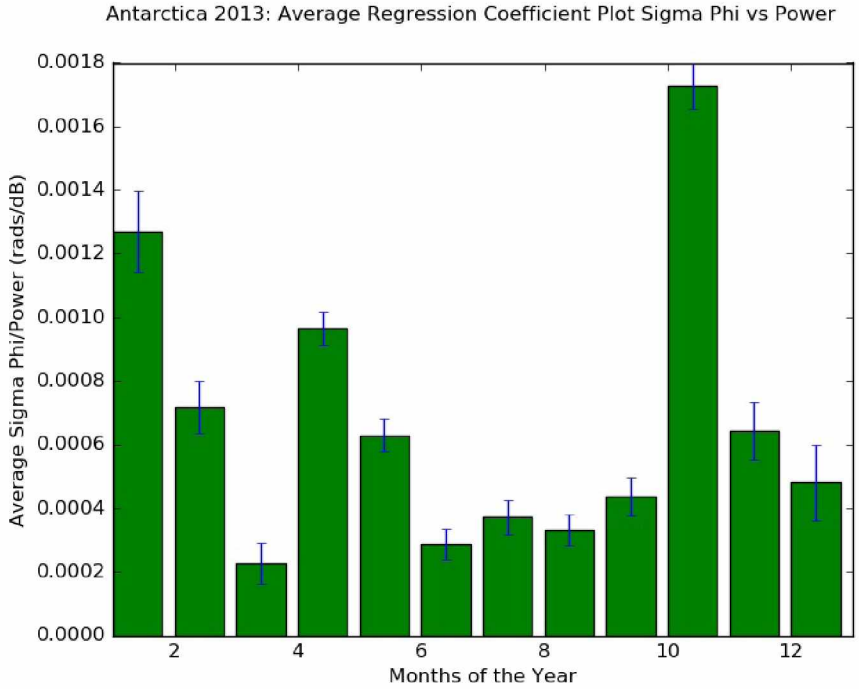

Figure 46: Antarctica average regression coefficient plot σ_φ vs Power for 2013

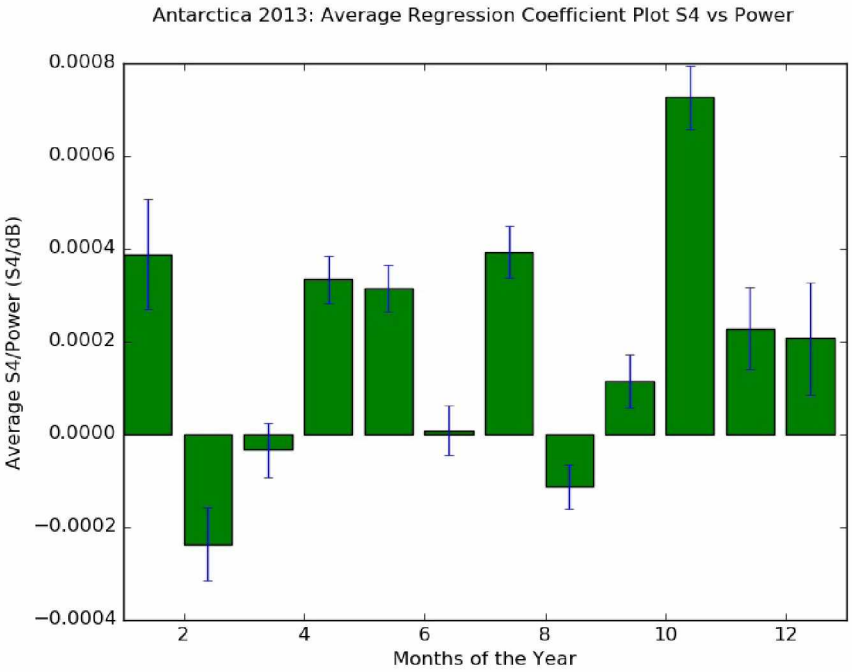

Figure 47: Antarctica average regression coefficient plot S_4 vs Power for 2013

Chapter 4 Conclusion

4.1 Thesis Overview

This thesis was undertaken to determine if there is a statistically significant correlation between SuperDARN and GPS scintillation data. Work by other researchers who analyzed a single day or groups of days when higher than average solar weather occurred [11] indicated some correlation between the two data sets. Their analysis showed that during the highest days of solar activity when the GPS scintillation variables increase there can be a corresponding increase in the SuperDARN variables of power and/or velocity. This thesis examined the daily effects from a large database to identify if the correlation seen within that research could be upheld for a broad range of conditions at polar latitudes.

This was done by analyzing daily SuperDARN data collected at northern and southern polar latitudes to identify if this data can be used to find the types of irregularities that affect GPS transmissions. The evaluation was done because the majority of GPS receivers that calculate GPS scintillation values are located on land and near population centers. Because of these receivers' locations the polar latitudes lack significant coverage. The SuperDARN network however, covers a large portion of the polar latitudes and could potentially supplement the gaps in GPS scintillation receiver coverage.

The data used for this thesis came from four separate sources, grouped by their northern or southern locations. The northern SuperDARN location is at Kodiak, Alaska. Six GPS scintillation receivers are located at Poker Flat, Alaska. The southern SuperDARN location is at South Pole, Antarctica. One GPS scintillation receiver is located at McMurdo, Antarctica. The data that was analyzed was collected during the years 2013 through 2015. Due to each location's instrument availability, differing amounts of daily data were collected.

4.2 Summary of Results

The bar graphs show when each GPS instrument registered scintillation or when a SuperDARN receiver registered an irregularity within a shared field of view. Within the Antarctica data most of the GPS data fell outside of the SuperDARN field of view. Because of this, a smaller percentage of the available SuperDARN points could be included. When evaluating the points from both locations, the data indicated that there are a large number of irregularities that were detected by SuperDARN but did not cause scintillation of the GPS

signals. Along with this, there is also a certain amount of irregularities that disrupt GPS signals that were not detected by SuperDARN. The time frame that has the highest percentage for both devices to register scintillation and irregularity simultaneously is between 20:00 and 23:00 local time. This particular investigation demonstrated the improbability of SuperDARN being able to infer the presence of irregularities that cause GPS signal scintillation. Further, investigation was done to examine the individual correlation between each of the SuperDARN parameter values and the GPS variables.

This investigation was first done using scatter plots, which did not show any identifiable pattern. Since no identifiable patterns were discerned, these plots were further analyzed by using histograms, binning each GPS scintillation value by SuperDARN value range. These histograms also did not display any distinct patterns. Next, the scatter plots were replotted as contour plots to better display the data density and the line fit was determined for both the mean and the mode of the binned data. The fitted lines did indicate that the GPS scintillation values increased as some of the SuperDARN parameter values increased, while scintillation decreased with increasing value of some other SuperDARN parameters. The slope values were then plotted as regression coefficients and their calculated uncertainty for each month of the year to show possible seasonal ties. There seems to be very little seasonal tie. It is interesting to note that SuperDARN's spectral width shows mostly negative regression coefficients. This indicates that most of the GPS scintillation data is within the lower values of spectral width thereby giving a negative regression coefficient. Another interesting factor is that the Antarctica data indicates that some of the lowest values of the regression coefficients occur during the months of April and August. During these months these latitudes are transitioning to and from full twilight.

The preceding results show that on a daily basis SuperDARN cannot be used as an identifying source for locating irregularities that have the potential for causing GPS scintillation at polar latitudes. There is some indication that while SuperDARN variables may have a higher probability of registering irregularities between 20:00 and 23:00 local time, it is not substantial enough to be regarded as reliable. Also, these results show the SuperDARN variables demonstrate a slight slope, but this is often negative. A negative slope indicates that as the

SuperDARN variables are increasing as the GPS scintillation values decrease. This shows that most GPS scintillation values are at the lower end of the SuperDARN values, making it extremely difficult to determine which values could indicate if scintillation will occur.

The previously mentioned paper [11] showed that it might be possible to use SuperDARN to identify the irregularities that cause GPS scintillations. The data analyzed in that study found very little correlation. There are three main possible reasons to explain why there are differences in the results. First, the previous research analyzed data from a single day with a high level of solar activity. This study analyzed data over a two-year period in which a variety of solar weather patterns occurred. Secondly, their study analyzed data from non-polar latitudes, while this study only analyzed data from polar latitudes. Lastly, the different analytical methods used to analyze the data might demonstrate different results even for the studies that show positive results.

4.3 Further Possible Investigations

By narrowing the scope of the project it may be possible to identify some correlation between GPS and SuperDARN if the graphing methods used in this thesis are employed to investigate a single day or multiple days of higher solar weather activity. This analysis may answer the questions that still remain within the study. One question to be investigated is whether the results become more distinguishable when larger than usual auroral activity occurs for a long duration? Secondly, if a bar graph is plotted for a single day, do the plotted peaks correspond with a greater value for the fitted slope found within the scatter plot occurring during corresponding hours?

Additionally, we know the effect of solar weather upon the ionosphere differs at various latitudes. Using this thesis's analytical methods, similar instruments at different latitudes could be used to see if the non-polar results are similar to or differ from the polar results identified in this thesis.

The last area that may warrant further research is based upon previous research by Garner [21]. Their research revealed that two identical baseline receivers reacted differently to the same ionospheric scintillation occurrence. This indicates that because the receiver's internal state can partially determine the impact of scintillation on its performance, an investigation

into each GPS receiver to identify its internal state could be helpful. To take this situation into account, for this thesis the different receivers were analyzed all at once with the assumption that the outliers' will be averaged out. By having the receiver's internal state examined it could correct any unknown margin of error that may have occurred within this thesis's results.

References

[1] R. D. Hunsucker and J. K. Hargreaves, The High-Latitude Ionosphere and its Effects on Radio Propagation, New York: Cambridge University Press, 2003.

[2] Shiksha, "10. Light - Reflection and Refraction," Shiksha, [Online]. Available: http://www.ekshiksha.org.in/eContent-Show.do?documentId=72. [Accessed 29 October 2016].

[3] I. Poole, "The Sun and HF radio propagation - A summary of the way in which the Sun affects ionospheric propagation (HF radio propagation) for two way radio communications, mobile radio communications, broadcasting, etc.," [Online]. Available: http://www.electronics-radio.com/articles/antennas-propagation/ionospheric/sun-hf-radio-propagation.php. [Accessed 16 September 2016].

[4] P. D. C. Stolle, "High Latitude Plasma Convection," GFZ, 21 July 2016. [Online]. Available: http://www.gfz-potsdam.de/en/section/earths-magnetic-field/topics/ionosphere-and-upper-atmosphere/high-latitude-plasma-convection/. [Accessed 15 September 2016].

[5] R. T. Tsunoda, "High-Latitude F Region Irregularities: A Review and Synthesis," *Reviews of Geophysics,* vol. 26, no. 4, pp. 719-760, 1988.

[6] Zytrax, "Tech Stuff- Wireless - Fresnel Zones and their effect," 21 October 2015. [Online]. Available: http://www.zytrax.com/tech/wireless/fresnel.htm. [Accessed 16 September 2016].

[7] P. M. Kintner, B. M. Ledvina and E. R. de Paula, "GPS and ionospheric scintillations," *Space Weather,* vol. 5, pp. 1-23, 2007.

[8] K. C. Yeh and C.-H. Liu, "Radio wave scintillations in the ionosphere," *Poceedings of the IEEE 70,* pp. 324-360, 1982.

[9] M. C. Kelly, The Earth's Ionosphere; Plasma Physics and Electrodynamics, Academic Press, Inc., 1989.

[10] S. Basu, E. J. Weber, T. W. Bullett, M. J. Keskinen, E. MacKenzie, P. Doherty, R. Sheehan, H. Kuenzler, P. Ning and J. Bongiolatti, "Characteristics of plasma structuring in the cusp/cleft

region at Svalbard," *Radio Sci.,* no. 33, pp. 1885-1900, 1998.

[11] P. Prikryl, R. Ghoddousi-Fard, B. S. R. Kunduri, E. G. Thomas, A. J. Coster, P. T. Jayachandran, E. Spanswick and D. W. Danskin, "GPS phase scintillation and proxy index at high latitudes during a moderate geomagnetic storm," *Ann. Geophys.,* vol. 31, pp. 805-816, 2013.

[12] J. Kindrade, C. N. Mitchell, N. D. Smith, Y. Ebihara, A. T. Weatherwax and G. S. Bust, "GPS phase scintillation associated with optical auroral emissions: FIrst statistical results from the geographic South Pole," *Journal of Geophysical Research: Space Physics,* vol. 118, pp. 2490-2502, 2013.

[13] R. A. Greenwald, K. B. Baker, R. A. Hutchins and C. Hanuis, "An HF phased-array radar for studying small-scale structure in the high-latitude ionosphere," *Radio Science,* vol. 20, no. 1, pp. 63-79, 1985.

[14] A. S. Rodger and T. J. Rosenberg, "Riometer and HF rdar signatures of polar patches," *Radio Science,* vol. 34, no. 2, pp. 501-508, 1999.

[15] B. W. O'Hanlon, M. L. Psiaki, T. E. Humphreys, G. Crowley and G. S. Bust, "CASES: A smart compact GPS software receiver for space weather monitoring, in Proceedings of the 24th International Technical Meeting of the Satellite Division of the Institute of Navigation," *Inst. of Nav.,* pp. 2745-2753, 2011.

[16] K. B. Deshpande, G. S. Bust, C. R. Clauer, H. Kim, J. E. Macon, T. E. Humphreys, J. A. Bhatti, S. B. Musko, G. Crowley and A. T. Weatherwax, "Initial GPS scintillation results from CASES receiver at South Pole, Antarctica," *Radio Sci.,* vol. 47, no. 5, p. RS5009, 2012.

[17] S. Datta-Barua, Y. Su, K. Deshpande, D. Miladinovich, G. S. Bust, D. Hampton and G. Crowley, "First light from a kilometer-baseline Scintillation Auroral GPS array," *Geophys. Res. Lett.,* vol. 42, pp. 3639-3646, 2015.

[18] J. A. Klobuchar, "Ionospheric Time-Delay Algorithm for Single-Frequency GPS Users," *IEEE transactions on aerospace and electronic systems,* Vols. AES-23, no. 3, pp. 325-331, 1987.

[19] M. L. El-Gizawy, Development of an ionosphere monitoring technique using GPS measurements for high latitudes GPS users, National Library of Canada, 2003.

[20] L. Alfonsi, L. Spogli, G. De Franceschi, V. Romano, M. H. O. Aquino and A. Dodson, "Climatology of GPS ionospheric scintillations over high and mid-latitude European regions," *Ann. Geophys.,* vol. 27, pp. 3429-3437, 2009.

[21] T. W. Garner, R. B. Harris, J. A. York, C. S. Herbster, C. F. Minter III and D. L. Hampton, "An auroral scintillation observation using precise, collected GPS receivers," *Radio Science,* vol. 46, no. 1, p. n/a, 2011.